



Surface wave tomography of the western United States from ambient seismic noise: Rayleigh and Love wave phase velocity maps

Journal:	<i>Geophysical Journal International</i>
Manuscript ID:	GJI-07-0228.R2
Manuscript Type:	Research Paper
Date Submitted by the Author:	22-Dec-2007
Complete List of Authors:	Lin, Fan-Chi; University of Colorado at Boulder, Physics Moschetti, Morgan; University of Colorado at Boulder, Physics Ritzwoller, Michael; University of Colorado at Boulder, Physics
Keywords:	ambient noise, Crustal structure, Surface waves, Tomography, cross-correlation, Green's function, western United States

1
2
3
4 **Surface wave tomography of the western United States from**
5
6
7 **ambient seismic noise: Rayleigh and Love wave phase velocity maps**
8
9

10
11
12
13 **Fan-Chi Lin, Morgan P. Moschetti, and Michael H. Ritzwoller**
14
15

16
17
18
19 **Center for Imaging the Earth's Interior**
20 **Department of Physics**
21 **University of Colorado at Boulder**
22 **Boulder, CO 80309-0390 USA**
23 **linf@colorado.edu, (303 492 0985)**
24
25
26
27
28
29
30
31
32
33
34
35
36
37
38
39
40
41
42
43
44
45
46
47
48
49
50
51
52
53
54
55
56
57
58
59
60

Peer Review

Abstract

We present the results of Rayleigh wave and Love wave phase velocity tomography in the western United States using ambient seismic noise observed at over 250 broadband stations from the EarthScope/USArray Transportable Array and regional networks. All available three-component time series for the 12-month span between 1 November 2005 and 31 Oct 2006 have been cross-correlated to yield estimated empirical Rayleigh and Love wave Green's functions. The Love wave signals were observed with higher average signal-to-noise ratio (SNR) than Rayleigh wave signals and hence cannot be fully explained by the scattering of Rayleigh waves. Phase velocity dispersion curves for both Rayleigh and Love waves between 5 and 40 sec period were measured for each inter-station path by applying frequency-time analysis. The average uncertainty and systematic bias of the measurements are estimated using a method based on analyzing thousands of nearly linearly aligned station-triplets. We find that empirical Green's functions can be estimated accurately from the negative time derivative of the symmetric component ambient noise cross-correlation without explicit knowledge of the source distribution. The average travel time uncertainty is less than 1 sec at periods shorter than 24 sec. We present Rayleigh and Love wave phase speed maps at periods of 8, 12, 16, and 20 sec. The maps show clear correlations with major geological structures and qualitative agreement with previous results based on Rayleigh wave group speeds.

1. Introduction

Surface-wave tomography using ambient seismic noise, also called ambient noise tomography (ANT), is becoming an increasingly well established method to estimate short period (< 20 sec) and intermediate period (between 20 and 50 sec) surface wave speeds on both regional (Sabra et al., 2005a; Shapiro et al., 2005; Kang and Shin, 2006; Yao et al., 2006; Lin et al., 2007; Moschetti et al., 2007) and continental (Yang et al., 2007; Bensen et al., 2007b) scales. The applicability of the method at long periods (> 50 sec) is also now receiving more attention (e.g., Yang et al., 2007; Bensen et al., 2007b). In these studies, Rayleigh wave Green's functions between station-pairs are estimated by cross-correlating long time-sequences of ambient noise recorded simultaneously at both stations. These studies have established that, within reasonable tolerances, the measurements are repeatable when performed in different seasons, the Green's functions agree with earthquake records, dispersion curves agree with those measured from earthquakes, and the resulting tomography maps cohere with known geological structures such as sedimentary basins and mountain ranges. Applied to regional array data, such as the EarthScope/USArray Transportable Array (TA), PASSCAL experiments, or the Virtual European Broadband Seismic Network, the resulting dispersion maps display higher resolution and are

1
2
3
4 obtained to much shorter periods than those typically derived from teleseismic earthquakes. This
5
6
7 holds out the prospect to infer considerably higher resolution information about the crust and
8
9
10 uppermost mantle over extended regions.
11
12
13
14
15

16
17 To date, these studies have concentrated exclusively on Rayleigh waves and predominantly have
18
19 used the estimated empirical Green's functions to obtain only measurements of group speed. Yao
20
21 et al. (2006) was the first to use the empirical Green's functions to estimate the Rayleigh wave
22
23 phase speed. The two principle purposes of this paper are, first, to investigate the extension of
24
25 ambient noise tomography to Love waves and, second, to make phase measurements in the
26
27 western United States. In so doing, we use data from the EarthScope/USArray TA combined with
28
29 other regional networks in the western United States. From its inception until 31 October 2006,
30
31 over 250 TA stations were deployed in this region and operated for various lengths of time
32
33
34
35
36
37
38
39
40
41 (Figure 1). Moschetti et al. (2007) have used these stations recently to obtain Rayleigh wave
42
43 group velocity maps at periods from 8 to 40 sec using ANT. We explicitly extend this study to
44
45 phase velocity measurements and also show for the first time that Love wave dispersion also can
46
47
48
49
50
51 be measured from ambient noise and used to produce tomographic maps.
52
53
54
55

56
57 Although coda wave studies (Campillo & Paul, 2003; Paul et al, 2005) demonstrated that Love
58
59
60

1
2
3
4 wave signals could also be extracted from the diffusive wave field, early ambient noise studies
5
6
7 focused on Rayleigh waves at the expense of Love waves because of the higher locally generated
8
9
10 noise on the horizontal components and general belief that the ambient noise source would be
11
12
13 ineffective at directly generating Love waves. Numerous ambient noise source studies (e.g., Rhie
14
15
16 and Romanowicz, 2004, 2006; Stehly et al., 2006; Yang and Ritzwoller, 2007) have concluded
17
18
19 that coupling between ocean waves and the shallow seafloor produces long-range coherent noise
20
21
22 on the vertical component. It has been believed, however, that it is more difficult to couple ocean
23
24
25 waves with horizontal motions of the seafloor, which would make Love wave generation less
26
27
28 efficient than that of Rayleigh waves. We show here that, in fact, Love waves appear clearly on
29
30
31 the transverse-transverse cross-correlations between most station pairs, at least at periods shorter
32
33
34 than 20 sec.
35
36
37
38
39
40

41 The ability to make both Rayleigh and Love wave dispersion measurements at periods shorter
42
43
44 than ~20 seconds is important if radial anisotropy (the bifurcation of V_{sv} and V_{sh}) in the crust is
45
46
47 to be observed. Shapiro et al. (2004) inferred strong radial anisotropy in the Tibetan crust, which
48
49
50 they argued is caused by on-going crustal deformation. This inference is based on observing a
51
52
53 discrepancy in the dispersion characteristics of Rayleigh and Love waves at periods for which
54
55
56 the waves are sensitive to the crust. The thick crust of Tibet means that surface waves retain
57
58
59
60

1
2
3
4 sensitivity to crustal structures to much longer periods than almost everywhere else in the world.

5
6
7 For a crustal Rayleigh-Love discrepancy to be observed across the western US, for example,
8
9
10 where the average crustal thickness is less than half that of Tibet, Rayleigh and Love wave
11
12
13 dispersion should be obtained to periods down to at least 10 sec. Such periods are attenuated
14
15
16 strongly from distant earthquakes and are largely unobservable, but are readily observed with
17
18
19 ambient noise.
20
21

22
23
24
25
26 Past work also has concentrated on group rather than phase velocities for a number of reasons,
27
28
29 perhaps most importantly because the “initial phase” of ambient noise cross-correlation was not
30
31
32 well understood and has been the subject of some speculation and confusion. Here we borrow the
33
34
35 term “initial phase” used in traditional earthquake analysis. Although the “initial phase” here is
36
37
38 purely caused by the inhomogeneity of the noise source distribution, it does share the same
39
40
41 mathematic form and meaning in the context of describing the estimated Green’s function, as we
42
43
44 will show. Theoretical work done by Lobkis & Weaver (2001), Roux et al. (2005), Sabra et al.
45
46
47 (2005b), and Snieder (2004) suggested that phase information in the surface-wave Green’s
48
49
50 function can be recovered from the negative time derivative of the symmetric cross-correlation
51
52
53 under the assumption of a spatially homogeneous ambient-noise source distribution. (The
54
55
56 “symmetric component cross-correlation” or “symmetric signal” is the average of the
57
58
59
60

1
2
3
4 cross-correlation at positive and negative correlation lag times.) Under this assumption, Yao et al.
5
6
7 (2006) presented the first phase speed tomography based on ambient noise over south-east Tibet.
8
9
10 However, how this assumption may alter, degrade or break-down given the inhomogeneous
11
12 distribution of ambient noise sources on earth has been unclear. The inhomogeneous distribution
13
14 of noise sources is seen clearly by comparing the positive and negative lags of the
15
16 cross-correlations (e.g., Lin et al., 2007). This type of observation is the basis for recent studies
17
18 aimed at characterizing ambient noise sources (e.g., Stehly et al., 2006; Yang & Ritzwoller,
19
20 2007). Yao et al. (2006) have also suggested that an inhomogeneous source distribution may
21
22 account for part of the 1% – 3% inconsistency they observed between phase velocity
23
24 measurements made by the ambient noise method and the traditional earthquake-based
25
26 two-station method between periods of 20 - 30 sec.
27
28
29
30
31
32
33
34
35
36
37
38
39
40

41 Phase velocity measurements are desirable for the following reasons. First, as we show, the
42
43 uncertainty of the phase velocity measurement is much smaller than that of the group velocity
44
45 measurement. Second, within the same period band, phase velocity has a deeper sensitivity
46
47 kernel and, therefore, constrains deeper velocity structures. Third, the dispersion relation for
48
49 group velocity can be calculated from the dispersion relation for phase velocity, but the converse
50
51 is not true.
52
53
54
55
56
57
58
59
60

1
2
3
4
5
6
7
8 In this paper, we address whether robust phase velocity measurements can be obtained from
9
10 ambient noise without explicit knowledge of the source distribution. We use an empirical
11
12 three-station method, discussed in section 4.2, to test this hypothesis and also to identify
13
14 systematic errors and the average uncertainty of real phase velocity measurements. Several
15
16 previous studies have used the seasonal variability of the measurement to estimate their
17
18 uncertainty (e.g., Lin et al., 2007; Bensen et al., 2007a; Yang et al., 2007). Our method, however,
19
20 avoids the possibility of repeated false measurements and systematic error. Synthetic
21
22 cross-correlations based on different source distributions, discussed in Section 6.2, suggest that
23
24 the “initial phase” of the estimated Green’s function would be approximately zero if the source
25
26 distribution were to vary smoothly over the constructive interference region. Combined with the
27
28 result of the three-station method, we show that even though ambient noise sources have an
29
30 inhomogeneous azimuthal distribution, ambient noise is distributed sufficiently homogeneously
31
32 so that no additional phase shift is required in the estimated Green’s function to account for
33
34 irregularities in the source distribution.
35
36
37
38
39
40
41
42
43
44
45
46
47
48
49
50
51
52
53
54
55
56
57
58
59
60

We emphasize here that the only difference between ambient noise seismology and earthquake based seismology is the method used to obtain the waveforms used in the analysis. We

1
2
3
4 extensively use terms borrowed from traditional earthquake seismology, such as “initial phase”,
5
6
7 “far field approximation”, and “signal-to-noise ratio”, to analyse and describe the estimated
8
9
10 Green’s function obtained by the cross-correlation of the ambient noise because these terms have
11
12
13 the same meaning in this context.
14
15
16
17
18
19

20 The outline of this paper is as follows. We describe the method to obtain the estimated Green’s
21
22 functions for both Rayleigh and Love waves in section 2. Evidence for the existence and
23
24 retrievability of Love waves is presented in section 3. In section 4, we describe the method used
25
26 to obtain the phase velocity measurements and the three-station method is developed to estimate
27
28 the systematic errors and the average uncertainty of the measurements. Tomography maps at
29
30 periods of 8, 12, 16, and 20 sec for both Rayleigh and Love wave phase speeds are presented in
31
32 section 5. Throughout the paper, the straight ray theory is used and we focus on phase velocity
33
34 measurements between periods of 8 and 24 sec, where the highest signal-to-noise ratios are
35
36 observed, on average.
37
38
39
40
41
42
43
44
45
46
47
48
49
50

51 **2. Data Processing to Produce the Estimated Green’s Functions**

52
53
54

55 We analyzed continuous data from over 250 broadband stations in the western US (Figure 1)
56
57
58
59
60

1
2
3
4 recorded between 1 November 2005 and 31 October 2006. Data from all three components (East,
5
6
7 North, Vertical) were used, and cross-correlations between all possible pairs of components from
8
9
10 the two-stations were computed. The method to obtain the estimated Green's function is similar
11
12
13 to that described for Rayleigh waves by Bensen et al. (2007a). We summarize it briefly here with
14
15
16 a concentration on the Love wave data processing.
17

18
19
20 All data are processed on a daily basis and then are stacked (superposed and added together) later.
21
22
23

24
25 The mean, trend, and instrument response of the daily component (E, N, Z) seismograms are first
26
27
28 removed and band-pass filtered between periods of 5 sec and 100 sec. To speed up the process,
29
30
31 we do not rotate the components into the radial (R) and transverse (T) directions for each
32
33
34 station-pair until the component cross-correlations (E-E, E-N, N-N, N-E) are performed.
35
36
37

38
39
40 Earthquake signals and instrumental irregularities are then removed by temporal normalization
41
42
43 (Bensen et al., 2007a). In order to postpone the component rotation until after cross-correlation,
44
45
46 the East and North components are temporally normalized together. To achieve this, both
47
48
49 components are first band-pass filtered between 15 sec and 50 sec, a band that contains the most
50
51
52 energetic surface wave signals from earthquakes. For each time point, the mean of the absolute
53
54
55 value of each seismogram is computed in the 128 second window centered on that point. The
56
57
58
59
60

1
2
3
4 values of the East and North components are compared, and the larger is used to define the
5
6
7 inverse weight for that time point. That weight is then applied to both the North and East
8
9
10 component time-series band-passed between 5 sec to 100 sec. This process effectively suppresses
11
12
13 earthquake signals and is commutative with the rotation operator.
14
15
16
17
18
19
20
21

22 After temporal normalization, the signals are whitened in frequency. Before whitening, ambient
23
24 noise is most energetic in the microseismic band below 20 sec period. Frequency whitening is
25
26
27 carried out to broaden the period band of the dispersion measurement. Again, to maintain the
28
29
30 commutativity of the rotation operator, the East and North signals are whitened together. To do
31
32
33 this, we first smooth the East amplitude spectrum by taking the average of the amplitude of
34
35
36 spectrum with a 0.01 Hz moving window in the frequency domain. Because the spectra of both
37
38
39 components are similar in shape, on average, we whiten both of them together simply by
40
41
42 weighting the East and North signals in the frequency domain by the inverse of this smoothed
43
44
45 East spectrum. In general, the phase dispersion measurement is not sensitive to the spectrum
46
47
48 variation but to the phase variation. Hence, this simple whitening process does improve the
49
50
51 spectral content and at the same time allows us to postpone the rotation step. Other methods,
52
53
54
55
56 such as weighting by the mean of the two spectra or their product, produce similar results. This
57
58
59
60

concludes the data preparation prior to cross-correlation.

North-North, North-East, East-East and East-North cross-correlations are calculated between every station-pair for each day-length record. We stack all available daily cross-correlations for each station-pair into one time-series to enhance the signal-to-noise ratio (SNR). Because all operators are commutative with the rotation operator, the transverse-transverse, transverse-radial, radial-radial, and radial-transverse cross-correlations between each station-pair can be calculated by a linear combination of those four components with coefficients related to the inter-station azimuth θ and back-azimuth ψ angles. These angles are defined by setting the first station as the “event” location and the second station as the receiver location so that the rotation is:

$$\begin{pmatrix} TT \\ RR \\ TR \\ RT \end{pmatrix} = \begin{pmatrix} -\cos\theta\cos\psi & \cos\theta\sin\psi & -\sin\theta\sin\psi & \sin\theta\cos\psi \\ -\sin\theta\sin\psi & -\sin\theta\cos\psi & -\cos\theta\cos\psi & -\cos\theta\sin\psi \\ -\cos\theta\sin\psi & -\cos\theta\cos\psi & \sin\theta\cos\psi & \sin\theta\sin\psi \\ -\sin\theta\cos\psi & \sin\theta\sin\psi & \cos\theta\sin\psi & -\cos\theta\cos\psi \end{pmatrix} \begin{pmatrix} EE \\ EN \\ NN \\ NE \end{pmatrix} \quad (1)$$

Note that both the radial components and the transverse components at both stations point to the same direction, respectively, under our notation, as shown in [Figure 2](#). The choice to rotate the North and East components into the transverse and radial components after cross-correlation makes the computation considerably more efficient and space saving. We have compared the

1
2
3
4 results from both cases and no differences are observed.
5
6
7
8
9
10

11
12 An example of the resulting cross-correlation between stations 116A and R06C is shown in
13

14
15 **Figure 3.** Both signals at positive and negative correlation lag times, respectively, are observed,
16

17
18 corresponding to waves propagating in opposite directions between the stations. A clear
19

20
21 difference in arrival time is observed between the waveforms on the transverse-transverse (T-T)
22

23
24 and radial-radial (R-R) cross-correlations. Signal arrival times on the vertical-vertical (Z-Z)
25

26
27 cross-correlation and the R-R cross-correlation are similar, and result from the Rayleigh wave.
28

29
30 The T-T cross-correlation exhibits the faster Love wave arrival. Although both the Z-Z and R-R
31

32
33 cross-correlations contain the same Rayleigh wave signal, the Z-Z cross-correlation generally has
34

35
36 a higher SNR. Hence, like others before us, we focus on using Z-Z cross-correlations for the
37

38
39 Rayleigh wave analysis.
40
41
42
43
44
45
46
47
48
49
50
51
52
53
54
55
56
57
58
59
60

Theoretical work done by Lobkis & Weaver (2001), Roux et al. (2005), Sabra et al. (2005b), and

Snieder (2004) showed that under a homogenous source distribution assumption, the relationship

between the ambient noise cross-correlation $C(t)$ and the estimated Green's function $G(t)$

between stations A and B can be expressed as:

$$\frac{dC_{AB}(t)}{dt} = -G_{AB}(t) + G_{BA}(-t) \quad -\infty \leq t < \infty. \quad (2)$$

This is equivalent to:

$$G_{AB}(t) = -\frac{dC_{AB}(t)}{dt} \quad 0 \leq t < \infty. \quad (3)$$

$$G_{BA}(t) = -\frac{dC_{AB}(-t)}{dt} \quad 0 \leq t < \infty. \quad (4)$$

By the spatial reciprocity of the Green's functions, $G_{AB}(t) = G_{BA}(t)$, we average the positive and negative lag signals to obtain the “symmetric-signal” of the cross-correlation and then use this symmetric-signal to obtain the final estimated Green's function:

$$G_{AB}(t) = -\frac{d}{dt} \left[\frac{C_{AB}(t) + C_{AB}(-t)}{2} \right] \quad 0 \leq t < \infty. \quad (5)$$

In most cases, this enhances the SNR and also effectively mixes the signals coming from opposite directions, which helps to reduce the effect of inhomogeneity of the source distribution.

The time-derivative and the sign-flip do not affect the group speed but do alter the signal phase and, hence, the measured phase speed. Without this operation, the symmetric cross-correlation can be thought of as the response due to an impulsive displacement. The traditional definition of

1
2
3
4 the Green's function, however, is the system response to an impulsive force, which is out of
5
6
7 phase with displacement by $\pi/2$. In the following, it will be important to remember this phase
8
9
10 difference between the cross-correlation and the empirical Green's function. In Bensen et al.
11
12
13 (2007a), the cross-correlation was mistakenly identified with the estimated Green's function.
14
15
16 Although both the phase and group velocity analyses based on the Green's function remain
17
18
19 correct in that paper, to get unbiased measurements, the cross correlation must first be
20
21
22 transformed to the empirical Green's function by using equation (5) above.
23
24
25
26
27
28
29
30

31 **3. Existence and Strength of Love waves in Ambient Noise**

32
33
34
35 **Figures 4a and 4b** show record sections centered at the station MOD (Modoc Plateau, CA), for
36
37
38 the Rayleigh wave (Z-Z) and the Love wave (T-T), respectively. Signals emerge at both positive
39
40
41 and negative correlation lags for Rayleigh and Love waves and Rayleigh waves clearly travel
42
43
44 slower than Love waves, as expected. Love waves, in fact, are commonly observed on
45
46
47 cross-correlations across the western US.
48
49
50
51
52
53
54

55
56 In order to quantify the strength of the signals, for each station-pair we calculate the spectral
57
58
59
60

1
2
3
4 signal-to-noise ratio (SNR) by computing the ratio of the signal peak in the predicted arrival
5
6
7 window to the root mean square (rms) of the noise trailing the arrival window, or “trailing noise”,
8
9
10 in each period band for the symmetric component cross-correlation. The prediction window is
11
12
13 defined by assuming that the waves travel between 2 to 5 km/s (Figure 3), and the noise window
14
15
16 starts 500 seconds after the prediction window and ends at 2700 seconds lag time. The SNR
17
18
19 provides information on the ratio between the coherent noise, the noise from common sources
20
21
22 recorded by both stations, and the incoherent noise, the noise from separate and independent
23
24
25 sources, in the ambient noise record. The resulting average SNR for all the station pairs with
26
27
28 inter-station distance larger than three wavelengths is shown in Figure 5, where a phase speed of
29
30
31 4 km/s is used to compute the wavelength here and elsewhere.
32
33
34
35
36
37
38
39

40 The most surprising feature observed in Figure 5 is that Love waves exhibit higher average SNR
41
42
43 than Rayleigh waves, especially between about 10 to 20 sec period. Because R-R and T-T
44
45
46 cross-correlations have very similar background noise or trailing noise, as both of them result
47
48
49 from the horizontal components of the seismogram, the Love wave is relatively stronger than the
50
51
52 Rayleigh wave on the horizontal components of the ambient noise. Thus, Love waves cannot be
53
54
55 generated exclusively by the scattering of Rayleigh waves. Moreover, the SNR of the Rayleigh
56
57
58
59
60

1
2
3
4 wave for both the Z-Z and R-R cross-correlations exhibits two peaks that correspond to the 8 sec
5
6
7 (secondary) and 16 sec (primary) microseisms, respectively. On the other hand, the Love wave
8
9
10 only shows a single peak around a period of 14 sec which suggests that the origin of Rayleigh
11
12
13 and Love waves may differ in some way.
14
15
16
17
18
19
20
21

22 The SNR drops rapidly for the Love waves above 20 sec period, in contrast with the slow
23
24 drop-off in SNR for the Rayleigh waves on the Z-Z component. However, on the R-R component,
25
26 the Rayleigh wave SNR remains lower than that of the Love wave up to 40 sec period where
27
28 little signal is detected. This indicates that the horizontal components of the seismograms are
29
30 heavily contaminated by incoherent local noise, such as tilting by local pressure variations. The
31
32 drop-off of SNR of Love waves above 20 sec period may, therefore, arise from the growth of
33
34 incoherent local noise rather than the decay of the signal with increasing period. Further
35
36 investigation of the physical mechanisms as well as the locations of the source of Love wave
37
38 ambient noise is important to address, but is beyond the scope of this paper.
39
40
41
42
43
44
45
46
47
48
49
50
51
52
53
54

55 **4. Phase Velocity Measurement**

56
57
58
59
60

1
2
3
4
5
6
7
8
9 All data processing described hereafter begins with the estimated Green's functions obtained
10
11 from the symmetric component of the cross-correlations by applying a negative time-derivative.
12
13
14 We used the Z-Z and T-T cross-correlations to obtain the estimated Rayleigh and Love wave
15
16
17 Green's functions for each station pair. With the choice of the direction we made on the
18
19 transverse component (Figure 2), the Rayleigh and Love wave Green's functions have the same
20
21 form and the same phase velocity analysis can be applied to both Rayleigh and Love waves.
22
23
24
25
26
27
28
29
30
31

32 **4.1 Frequency-Time Analysis**

33
34
35

36 We obtained the Rayleigh wave and Love wave phase velocity dispersion curves by automated
37
38 frequency-time analysis (FTAN) (Bensen et al., 2007a). First, FTAN applies a series of Gaussian
39
40 band-pass filters to the estimated Green's function. The resulting real waveform $f(t)$ at each
41
42 period can be combined with the imaginary waveform $+iF_H(t)$ to form a complex
43
44
45 function $A(t)\exp[i\varphi(t)]$, where $F_H(t)$ is the Hilbert transform of $f(t)$, $A(t)$ is the envelope function,
46
47 and $\varphi(t)$ is the phase function. We note that the choice of the positive sign of $+iF_H(t)$ results in a
48
49 decrease of phase with an increase in time. This choice is somewhat arbitrary; but must be
50
51
52
53
54
55
56
57
58
59
60

consistent with the theoretical phase as shown in the equation (6) below. After obtaining the envelope and phase functions, the group travel time, t_{max} , is measured directly as the peak of the envelope function, and the group velocity is simply r/t_{max} , where r is the distance between the two stations. The corresponding instantaneous frequency at t_{max} is determined by taking $\omega =$

$\left[\frac{\partial \varphi(t)}{\partial t} \right]_{t=t_{max}}$, which deviates from the center frequency of the Gaussian band-pass filter slightly.

Theoretically, for an instantaneous frequency ω the phase of the estimated Green's function observed at time t can be expressed as:

$$\varphi(t) = kr - \omega t + \frac{\pi}{2} - \frac{\pi}{4} + N \cdot 2\pi + \lambda \quad N \in Integer, \lambda \in Re \quad (6)$$

where k is the wave number, $\pi/2$ is the phase shift from the negative time-derivative, $-\pi/4$ is the phase shift due to the interference of a homogeneous source distribution (discussed further in section 6.2 below), $N \cdot 2\pi$ is the intrinsic phase ambiguity of phase measurement, and λ is the source phase ambiguity term or "initial phase" that arises from the uncertainty of the source distribution in addition to other factors.

Note that under the theoretical expectation for the Green's function, which is the displacement response due to a point force impulse, the $\pi/2$ phase shift accounts for the phase shift between the

1
2
3
4 displacement and the force and the $-\pi/4$ phase shift is the asymptotic remnant of the Bessel
5
6
7 function under the far-field approximation. Further discussion on how the $-\pi/4$ phase term arises
8
9
10 and how λ may depend on the source distribution appears in section 6.2.
11
12

13
14
15
16
17
18 From equation (6), the phase velocity c when measured on the empirical Green's function is
19
20
21 given by
22
23

$$c = \frac{\omega}{k} = \frac{r\omega}{\left[\varphi(t_{\text{max}}) + \omega t_{\text{max}} - \frac{\pi}{4} - N \cdot 2\pi - \lambda \right]} \quad (7)$$

24
25
26
27
28
29
30
31 and the phase travel time is r/c . In equation (4), N and λ are still unknowns, however. In order to
32
33
34 obtain a reliable, unambiguous phase velocity measurement, both N and λ are needed. As we will
35
36
37 discuss, N is an integer that can be determined unambiguously in the vast majority of cases. The
38
39
40 source phase ambiguity factor λ , however, can be any real number and also can be frequency
41
42
43 dependent. It is, therefore, more difficult to constrain, and its determination is the subject of
44
45
46 section 4.2.
47
48
49
50
51
52
53
54

55 We determined N based on a two-step process. First, we compare the resulting measurement with
56
57
58
59
60

1
2
3
4 previous phase velocity studies based on earthquake data at long periods (> 20 s) to obtain the
5
6 preliminary dispersion curve. Above 20 second period, the surface wave phase velocity variation
7
8 is relatively small and N off by one can be clearly distinguished when the distance is small ($<$
9
10 1000 km). **Figure 6a** shows an example of dispersion curves obtained from cross-correlation of
11
12 data from stations CVS and VES in California with various different N values and with $\lambda=0$.
13
14 Here, we used the average phase velocity curve determined by Yang & Forsyth (2006) in
15
16 Southern California as the reference curve for the Rayleigh waves. No suitable Love wave
17
18 reference curve exists, so we increased the Rayleigh wave curve by 9% to give the Love wave
19
20 reference. By applying a smoothness constraint to the dispersion curves, N at shorter periods ($<$
21
22 20 s) can also be resolved.
23
24
25
26
27
28
29
30
31
32
33
34
35
36
37
38
39

40 The second step is basically repeating the first step but using a revised reference phase velocity
41
42 curve between each station pair. To get a more accurate reference curve, we used the preliminary
43
44 dispersion measurements obtained using the method described above combined with the
45
46 selection criteria described in section 5 to invert for preliminary phase speed maps for periods
47
48 between 6 and 28 seconds. We used these maps to estimate the dispersion curves for every
49
50 station pair which we then used as the reference curves to redetermine N . This second step
51
52
53
54
55
56
57
58
59
60

1
2
3
4 effectively resolves the 2π ambiguity that cannot be resolved in the first step either due to the
5
6
7 lack of good signal at long periods or when the station-pair is at a long distance. Perhaps more
8
9
10 importantly, this step makes dispersion measurement a self-consistent process and less dependent
11
12
13 on a priori assumptions. More Love wave measurements, but fewer than 4%, were changed after
14
15
16 the second step than Rayleigh wave, probably due to the degradation of SNR at long periods.
17
18

19
20 **Figure 6b** shows an example of Love wave measurement between stations A04A (Legoe Bay,
21
22 WA) and 109C (Camp Elliot, CA). Due to the extremely long distance (> 1800 km) and the lack
23
24
25 of good measurement above 20 second, the preliminary measurement had N off by one, but is
26
27
28 corrected after the second step. Although this two-steps process effectively allows for
29
30
31 identification of the appropriate N for most cases, the same method does not work for λ .
32
33
34
35
36
37
38
39
40

41 As an example of the resulting Rayleigh and Love wave phase velocity measurements through
42
43 different geological features, **Figure 7** shows two sets of symmetric component cross-correlations
44
45
46 and the resulting phase velocity dispersion curves. The path between O01C (Eel River
47
48 Conservation Camp, CA) and R04C (Big Horse Ranch, CA) goes through the Sacramento Basin
49
50
51 and the path between ORV (Oroville Dam, CA) and TIN (Tinemaha, CA) goes through the Sierra
52
53
54
55
56 Nevada. A clear velocity contrast at short periods (<15 sec) due to the variation of sediment
57
58
59
60

1
2
3
4 thickness is observed between O01C–R04C and ORV–TIN. The rapid increase of the phase
5
6
7 velocity with period for O01C–RO4C between 10–20 sec is a characteristic feature of thin crust.
8
9
10 On the other hand, an almost flat dispersion curve, such as that for ORV–TIN shown here,
11
12
13 usually represents a thicker crust. In both cases, the Love wave measurements consistently
14
15
16 exhibit higher phase velocities than the Rayleigh wave measurements and approach our
17
18
19 preliminary reference models at long periods.
20
21
22
23
24
25
26
27

28 **4.2 Three-Station Method: Determination of λ**

29
30
31
32 Theoretical studies have predicted that the “initial phase”, λ , should equal zero under the
33
34
35 assumption of a homogeneous source distribution (e.g., Sneider 2004; Roux et al. 2005). There is,
36
37
38 however, strong observational evidence that the strength of ambient noise is azimuthally
39
40
41 heterogeneous (e.g., Shapiro et al., 2006; Stehly et al., 2006; Yang and Ritzwoller, 2007). It is,
42
43
44 therefore, necessary to determine the value of λ empirically. To do this, we compare the phase
45
46
47 travel time (or delay) between station-triples that are nearly aligned along the same great-circle.
48
49
50 In general, such station-triples are hard to find, but the TA component of EarthScope/USArray
51
52
53 has been laid out approximately on a square grid and many such near station-triples exist. It is
54
55
56 the ideal network configuration to resolve this problem.
57
58
59
60

1
2
3
4
5
6
7
8
9 The idea is as follows. Consider a station-triple that is composed of three nearly co-linear
10
11 stations A, B, and C, as shown in Figure 8a, where station B lies between stations A and C.
12
13
14 Stations A and B are separated by a distance d_2 , B and C are separated by a distance d_3 , and A
15
16 and C are separated by a distance d_1 . The distance d_1 is nearly but not identically equal to the
17
18 sum of the distances d_2 and d_3 . If there is no “initial phase” term for all cases (i.e., if $\lambda = 0$), then
19
20 the sum of the observed phase times taken on the short-legs, stations A-B and B-C, will
21
22 approximately equal the phase time observed on the long-leg; i.e., between the outside stations
23
24 A-C, assuming that the wave always propagates in a straight line. Thus, $t_1 \approx t_2 + t_3$. If, however,
25
26 there is a non-zero “initial phase” ($\lambda \neq 0$), there will be a difference between the sum of the phase
27
28 times on the short-legs and that on the long-leg: $t_1 \neq t_2 + t_3$. To interpret each individual
29
30 deviation is not practical. However, the bulk statistics can be interpreted to produce an estimate
31
32 of λ . In addition, this three-station method provides information about measurement
33
34 uncertainties and possible systematic bias.
35
36
37
38
39
40
41
42
43
44
45
46
47
48
49
50
51
52
53
54
55
56
57
58
59
60

In performing this analysis, the difference in distance between the sum of the two shorter legs
(d_2+d_3 in Figure 8a) and the longest leg (d_1 in Figure 8a) is limited to less than 20 km. Also, to

1
 2
 3
 4 limit ourselves to reliable velocity measurements but retain a sufficient number of measurements
 5
 6
 7 for statistical analysis, the following selection criteria are used. First, the distance between each
 8
 9
 10 station-pair in a triple must exceed 3 wavelengths to satisfy the far-field approximation. Again, a
 11
 12
 13 phase velocity of 4 km/s is used to estimate the wavelength. Second, the SNR at the period of
 14
 15
 16 interest must be greater than 17 for all three pairs of stations for the triple to be included in the
 17
 18
 19 analysis. We choose these two selection criteria both here and in the tomographic inversion
 20
 21
 22 following the analysis done by Bensen et al. (2007a), which removed most of the erroneous
 23
 24
 25 measurements. On top of that, we also limit the distance between each station-pair to no longer
 26
 27
 28 than 1000 km to avoid the most serious off-great-circle path and finite frequency effects.
 29
 30
 31
 32
 33
 34
 35
 36

37 The relationship between distance difference $(d_2+d_3)-d_1$, or Δd , and phase travel time difference
 38
 39
 40 $(t_2+t_3)-t_1$, or Δt , at a period of 18 sec for all the station-triples that satisfy the above conditions,
 41
 42
 43 40,782 in total, is plotted as an example in [Figure 8b](#). A clear trend is seen, with Δt increasing as
 44
 45
 46 Δd increases. To account for this slope, a corrected phase travel time difference $\Delta t'$ is computed
 47
 48
 49 as follows
 50
 51
 52

$$\Delta t' = \frac{d_1 \cdot (t_2 + t_3)}{d_2 + d_3} - t_1 \quad (5)$$

1
2
3
4 Here, $\frac{t_2 + t_3}{d_2 + d_3}$ can be considered as the average slowness for the wave traveling through d_2
5
6
7 and d_3 . The relationship between Δd and $\Delta t'$ is plotted in **Figure 8c**, where we have set $\lambda = 0$, and
8
9
10 the majority of the measurements aggregate near $\Delta t' = 0$. With the “initial phase” $\lambda = -\pi/4$, the
11
12
13 result is presented in **Figure 8d** for comparison. In this case, most of the $\Delta t'$ shift by 2.25 sec to
14
15
16 the right and the majority of the $\Delta t'$ clearly deviate from zero. This deviation indicates a
17
18
19 systematic bias in the measurement, in this case caused by the wrong value of λ . Only a few
20
21
22 points with $|\Delta t' - \overline{\Delta t'}| > 10$ sec are observed in **Figure 8c**, where $\overline{\Delta t'}$ is the mean of $\Delta t'$,
23
24
25 indicating that all the N values in equation (7) are chosen accurately. We have also performed the
26
27
28 same analysis after the first step of the dispersion measurement described above. Around 1% of
29
30
31 the total points were observed with $|\Delta t' - \overline{\Delta t'}| > 10$ sec which resulted from the wrong choice of
32
33
34 the N .
35
36
37
38
39
40
41

42 Results for the corrected travel-time difference between the long-leg and the sum of the two
43
44 shorter legs, $\Delta t'$, for the 12, 18, and 24 sec period Rayleigh waves and the 12 and 18 sec Love
45
46 waves are summarized with histograms in **Figure 9a-d**. The number of station-triples that pass
47
48 the selection criteria is too small to be considered statistically significant for the 24 sec Love
49
50
51 wave. The standard deviation (STDV) and the mean value of the Gaussian fit to these histograms
52
53
54
55
56
57
58
59
60

1
2
3
4 is summarized in **Table 1**. Results for “initial phase” $\lambda = 0$ and $-\pi/4$ are used again for
5
6
7 comparison. For both Rayleigh and Love waves, with $\lambda = -\pi/4$, the mean of the Gaussian fit
8
9
10 clearly deviates from zero and the deviation increases with period. On the other hand, the
11
12
13 deviation from zero is small with $\lambda = 0$ for all cases, although it tends to increase with period as
14
15
16 well. We believe that $\overline{\Delta t'}$ provides an upper bond on the expected bias in ambient noise
17
18
19 measurements caused by an inhomogeneous source distribution, which is between 0.1–0.3 sec
20
21
22 for Rayleigh waves and 0.2–0.4 sec for Love waves.
23
24
25
26
27
28

29 To further investigate the nature of these small deviations when $\lambda = 0$ is used, we have tried the
30
31
32 same analysis with different selection criteria. We find that the critical controlling parameter for
33
34
35 these small deviations is the maximum distance allowed. The smaller the distance allowed, the
36
37
38 smaller the deviations are. This is not surprising if we accept the fact that the straight ray
39
40
41 approximation becomes less robust when the path becomes longer and the principle of least time
42
43
44 will always guarantee the phase travel time of the longest path to be smaller than the sum of the
45
46
47 phase travel times of the two shorter paths. Including off-great-circle and finite-frequency effects
48
49
50 is beyond of the scope of this study, but we can conclude that by using $\lambda = 0$ the systematic bias
51
52
53 due to the inhomogeneous source distribution of the ambient noise is negligible.
54
55
56
57
58
59
60

1
2
3
4 We can also estimate the average uncertainty of the measurements from Table 1. If we assume
5
6
7 that the three phase travel times t_1 , t_2 , and t_3 are independent measurements, the average
8
9
10 uncertainty of each individual travel time measurement can then be estimated by $\frac{1}{\sqrt{3}} \sigma$, where σ
11
12
13 is the STDV in the Gaussian fit. The average phase time uncertainty increases with increasing
14
15
16 period as expected, but is less than 1 second for all cases. An uncertainty of less than half a
17
18
19 second would be difficult to attain because 1 sample per second time series are used in this study.
20
21
22 This estimation of the phase travel time uncertainty is independent of the repeatability of the
23
24
25 measurements at different times, which has been performed in other studies (e.g., Yang et al.,
26
27
28 2007; Bensen et al., 2007a), and provides a new way to estimate the average travel time
29
30
31 uncertainty. This uncertainty, however, is characteristic of the inter-station spacings used in this
32
33
34 study, and would be expected to grow with increasing inter-station distance.
35
36
37
38
39
40
41
42

43 The three-station method developed here confirms that $\lambda = 0$ is a good approximation for the
44
45
46 majority of the measurements and bias caused by an inhomogeneous source distribution is
47
48
49 minimal. The results also provide insight into the quality of the phase velocity measurements.
50
51

52 Overall, the phase travel time measurements in this study display a negligible systematic error
53
54
55 and an average uncertainty of less than 1 second for periods shorter than 24 sec. The implication
56
57
58
59
60

of these results for the distribution of ambient noise sources is discussed in section 6.2.

5. Phase Velocity Tomography for Rayleigh and Love Waves

The selection of the most reliable measurements for tomography is based on three criteria. First, the distance between two stations must be longer than 3 wavelengths to satisfy the far-field approximation. Again, 4 km/s is used as a rule-of-thumb to estimate the wavelength. This introduces an effective long-period cut-off of $r/12$ (in seconds) between stations separated by distance r in km. For example, stations separated by 120 km will not return measurements at periods greater than 10 sec. Second, the SNR must be higher than 17 at the period of interest. These two criteria are chosen following Bensen et al. (2007a). Third, each measurement must be coherent with other measurements as measured by its ability to be fit by a smooth tomographic map.

Figure 10 shows the number of measurements satisfying the first two selection criteria out of the 31,878 station-pairs for both Rayleigh and Love waves at different periods. The shapes of the curves are very similar to the average SNR curves shown in **Figure 5**. At periods above 20 sec,

1
2
3
4 both the R-R Rayleigh and T-T Love wave signals presumably have been obscured by high local
5
6
7 noise levels on the horizontal component of the seismogram. This limits the longest period of
8
9
10 Love wave tomography in this study to about 20 sec. The lower local noise on the vertical
11
12
13 component allows us to extend the tomography for Rayleigh waves to significantly longer
14
15
16 periods.
17

18
19
20
21
22
23
24
25 We inverted the phase velocity measurements for both Rayleigh and Love waves at 8, 12, 16, and
26
27
28 20 sec period for phase speed maps using the tomographic method described by Barmin et al.
29
30
31 (2001). The method estimates isotropic wave speed by minimizing a penalty function composed
32
33
34 of data misfit, model smoothness, and the perturbation \mathbf{m} to an input reference model,
35
36
37 \mathbf{m}_0 , weighted by local path density. Here, we used the average of all selected velocity
38
39
40 measurements at each period as our reference model \mathbf{m}_0 . The method effectively employs “fat
41
42
43 rays”, similar to the use of Gaussian beams. Although the result of our three-station method
44
45
46 indicates the existence of off-great-circle and finite frequency effect, the effect is in general small.
47
48
49 Ritzwoller et al. (2002) also showed that diffraction tomography with finite frequency sensitivity
50
51
52 kernels recovers similar structures to this version of ray theory at periods shorter than 50 sec in
53
54
55 most continental regions with dense path coverage. We have no reason to believe that more
56
57
58
59
60

1
2
3
4 sophisticated finite-frequency kernels would change the results presented here appreciably,
5
6
7 particularly in light of uncertainties in the shape of such kernels, the short periods considered
8
9
10 here, and the short inter-station paths compared to teleseismic path lengths. However, more
11
12
13 careful study needs to be done especially when considering the tomographic inversion including
14
15
16 the azimuthal anisotropy when the travel time effects of off-great-circle paths could prove to be
17
18
19 important.
20
21
22
23
24
25
26
27

28 **Figures 11a and 11c** show the typical path coverage for Rayleigh and Love waves, respectively,
29
30 in the inversion. **Figures 11b and 11d** show the resulting resolution maps estimated with the
31
32 method described by Barmin et al. (2001) with modifications presented by Levshin et al. (2005).
33
34
35 For each point on the map, the resolution surface resulting from the resolution kernel/matrix is fit
36
37 locally by a 2-D Gaussian function and twice the estimated standard-deviation is identified with
38
39
40 the estimated resolution. The resolution across most of the western US is smaller than 70 km,
41
42
43 approximately equal to the average inter-station spacing, as expected for good data coverage.
44
45
46
47
48
49
50
51
52
53
54

55 A third data selection criterion must be satisfied by the data. Using data satisfying the first two
56
57
58
59
60

1
2
3
4 criteria, we invert for a preliminary over-smoothed map at each period. All the measurements
5
6
7 with travel time residuals larger than 6 seconds were removed from the data set. This process
8
9
10 removed around 1.9%, 1.2%, 0.4%, and 0.2% of the data for the Rayleigh waves at 8, 12, 16 and
11
12
13 20 sec and 3.8%, 3.4%, 1.4% and 0.6% for the Love waves, respectively. More measurements
14
15
16 were removed at shorter periods, especially for the Love waves, mainly due to the larger velocity
17
18
19 variations that result from structural variations at shallow depth.
20
21
22
23
24
25
26
27

28 Examples of the resulting tomography maps are shown in [Figures 12 and 13](#). The tomography
29
30 maps at 8, 12, 16, and 20 sec for both Rayleigh waves and Love waves are shown. The black
31
32 contour plotted on each map encloses the region with an estimated resolution less than 100 km.
33
34
35 Any features outside this contour should be interpreted with caution.
36
37
38
39
40
41
42
43
44
45

46 The misfit of the tomography maps to the data is summarized in [Figure 14](#). The small standard
47
48 deviations (STDV) of the misfits indicate good coherence between the measurements, on
49
50 average. The gradual increase in STDV with decreasing period reflects stronger heterogeneity in
51
52 the shallower crust. The fit to the data is in general agreement with the uncertainties that result
53
54
55
56
57
58
59
60

1
2
3
4 from the 3-station analysis in section 4.2.
5
6
7

8 **6. Discussion**

9

10 **6.1 Phase velocity maps for Rayleigh and Love waves**

11
12
13
14
15
16

17 As an aid to guide the qualitative interpretation of the phase velocity maps, **Figure 15** displays
18 the radial sensitivity kernels for Rayleigh and Love waves based on PREM in which the ocean is
19 replaced by a sedimentary layer.
20
21
22
23
24
25
26
27
28
29
30

31 The 8 sec Love wave map is most sensitive to the upper 10 km of the crust and represents the
32 shallowest structure in all cases. The fast anomaly of the Sierra Nevada and the slow anomaly of
33 the Central Valley of California are the most profound features in the 8 sec Love wave map.
34
35
36
37
38
39
40
41
42
43
44

45 The 12 sec Love wave and 8 sec Rayleigh wave maps are both sensitive to slightly deeper
46 structures and image very similar features, as expected. Again, the fast anomaly of the Sierra
47 Nevada is seen, but the Central Valley anomaly starts to separate into the Sacramento Basin in
48 the north and the San Joaquin Basin in the south. The fast anomaly of the Cascade Range begins
49
50
51
52
53
54
55
56
57
58
59
60

1
2
3
4 to appear from northern California through Washington.
5
6
7
8
9

10
11
12 The 12 sec and 16 sec Rayleigh wave and 16 sec and 20 sec Love wave maps consistently
13 exhibit similar features. The major slow anomaly of the Central Valley region gradually
14
15 disappears with increasing period because the surface waves begin to sense the faster shear wave
16
17 speeds in the crystalline rocks in the underlying basement, and the slow shear wave speeds of the
18
19 sediment layer are compensated by higher velocities below. In the 20 sec Rayleigh wave map,
20
21 the opposite effect can be seen in the Sierra Nevada region. Due to relatively thick crust, the fast
22
23 anomaly at shorter periods gradually becomes less prominent at longer periods.
24
25
26
27
28
29
30
31
32
33
34
35
36
37
38

39 These results are in general agreement with previous studies. Moschetti et al. (2007) observed
40
41 the Rayleigh wave group velocity dispersion in the same region with ambient noise tomography.
42
43 In general, the phase velocity measurements are sensitive to slightly deeper structures compared
44
45 to group velocities at the same period. Comparing the 8 sec, 16 sec, and 24 sec Rayleigh wave
46
47 group velocity maps of Moschetti et al. (2007) with our 8 sec, 12 sec, and 20 sec Rayleigh wave
48
49 phase velocity maps, respectively, a striking similarity is observed. Also, there are very similar
50
51
52
53
54
55
56
57
58
59
60

1
2
3
4 features on our 25 sec Rayleigh wave map (not shown here) with the one reported by Yang and
5
6
7 Forsyth (2006) in Southern California, which was constructed using the two plane wave method
8
9
10 with teleseismic earthquakes. In Yao et al. (2006), a 1.5%–3% systematic bias between Rayleigh
11
12
13 wave phase velocities between 20–30 sec period measured by the ambient noise method and the
14
15
16 earthquake-based two station method was reported. We compare our mean speed in the Southern
17
18
19 California with that obtained by Yang and Forsyth (2006), the difference is less than 0.5%. We
20
21
22 suspect the systematic bias observed by Yao et al. (2006) is mostly due to bias in the traditional
23
24
25 two station method and perhaps too few earthquakes used. In the two station method, the
26
27
28 directionality of the incoming teleseismic wave is assumed to be parallel to the great-circle
29
30
31 connecting the station and the event. On the other hand, the two plane wave method used by
32
33
34 Yang and Forsyth (2006) does not assume this direction for the incoming wave.
35
36
37
38
39
40
41
42

43 **6.2 Implications for the Distribution of Ambient Noise Sources**

44
45
46
47 The source phase ambiguity term or “initial phase” λ in the equation (3) was introduced to
48
49
50 account for the phase shift due to a possibly azimuthally inhomogeneous distribution of ambient
51
52
53 noise sources. We discuss here how source distribution is expected to affect the phase of the
54
55
56 cross-correlation and then draw conclusions about the ambient noise source distribution from the
57
58
59
60

1
2
3
4 three-station method discussed in section 4.2.
5
6
7
8
9
10

11
12 In general, the ambient noise records at two separated stations contain both coherent and
13
14 incoherent noise. The coherent noise emanates from common sources recorded by both stations.
15
16 The incoherent noise, on the other hand, results from separated and independent sources. When
17
18 the cross-correlation is performed, this non-related incoherent noise in the seismograms
19
20 generates the background noise in the resulting cross-correlation. The signal in the
21
22 cross-correlation comes from the coherence noise. For a common source cross-correlation, when
23
24 a homogeneous medium is considered, the “initial phase” of this cross-correlation at a particular
25
26 instantaneous frequency is purely determined by the distance difference between the source and
27
28 the two stations. In consequence, source locations with the same “initial phase” will lie along
29
30 hyperbolas with foci at the two stations. **Figure 16** shows an example of the iso-phase hyperbolas
31
32 at 50 sec period with stations separated by 1000 km, where the “initial phase” of each
33
34 neighboring hyperbola differs by π . Over most of the region, the “initial phase” is sensitive to
35
36 even slight changes in the azimuth angle, so that when multiple sources are present, destructive
37
38 interference occurs. The areas with highly stable “initial phase” occur where the spacing between
39
40 the adjacent hyperbolas is large. These regions, where sources will interfere constructively, are
41
42
43
44
45
46
47
48
49
50
51
52
53
54
55
56
57
58
59
60

1
2
3
4 located on the outward sides of the two stations near the line connecting them. If sources were
5
6
7 located exclusively along the outward lines linking the two stations, then uniform constructive
8
9
10 interference would occur and instead of the 3D Green's function, a 2D Green's function would
11
12
13 be obtained. For this case, the $-\pi/4$ that appears in equation (7) would need to be removed or,
14
15
16 alternatively, the "initial phase" λ would need to be set to $\pi/4$. In contrast, for an azimuthally
17
18
19 homogeneous source distribution, the resulting constructive interference in the two outward areas
20
21
22 together with the destructive interference for sources elsewhere, results in a $-\pi/4$ phase shift in
23
24
25 the cross-correlation relative to if the sources are only located on the outgoing parts of the line
26
27
28 connecting the two stations. In this case, a 3D Green's function is obtained and this phase shift
29
30
31 corresponds to the $-\pi/4$ in equation (7); $\lambda = 0$ in this case. Analytical proof of this phase shift by
32
33
34 using the stationary phase approximation can be found in Sneider (2004).
35
36
37
38
39
40
41
42

43 Through our three station analysis, described in section 4.2 above, we concluded that with $\lambda=0$
44
45
46 systematic measurement bias is negligible, with an average travel time uncertainty of about 1
47
48
49 second. This sets an upper bound for the uncertainty of the phase ambiguity λ due to
50
51
52 inhomogeneities of the source distribution equal to about $\pi/10$ or one-twentieth of a cycle,
53
54
55 because measurement error also contributes to the uncertainty of the measurement. How this
56
57
58
59
60

1
2
3
4 small uncertainty of λ fits into the apparently inhomogeneous source distribution around the
5
6
7 globe is a nontrivial question. We present here three synthetic experiments based on different
8
9
10 source distributions to provide some insight.
11

12
13
14
15
16
17
18 In Case 1, synthetic sources are distributed randomly in a 5000 km \times 5000 km square area and
19
20 the receivers are placed 1000 km apart, as shown in Figure 16. In this case, with $\lambda = 0$, our
21
22 measurement procedure is expected to return the input phase velocity. In Case 2, the sources are
23
24 randomly distributed, but are confined to the line connecting the stations. Instead of $\lambda = 0$, we
25
26 expect to measure the correct phase velocity only when λ is set equal to $+\pi/4$, which can be
27
28 derived from equation (6). In Case 3, the synthetic sources are randomly distributed in the grey
29
30 area showed in Figure 16 and we have no priori knowledge of λ . The first two cases here are
31
32 focused on confirming the method and our idea of “initial phase”, and the third case is what we
33
34 consider to be a more realistic model of the actual ambient noise source distribution. We choose
35
36 3 km/s as an input phase velocity for a non-dispersive, non-attenuative homogeneous medium.
37
38 Each synthetic source emits a Gaussian-like wavefront with a 3 second width propagating
39
40
41
42
43
44
45
46
47
48
49
50
51
52
53
54
55
56
57
58
59
60 outward with a random initial time and random polarity.

1
2
3
4 The resulting 5-100 sec band-pass cross-correlation functions for all cases are shown in **Figure**
5
6
7 **17a**. Clear signals are observed on all three cross-correlations. In Case 3, the signals are only
8
9
10 observed at positive lag time due to the asymmetry of the source distribution; all sources are to
11
12
13 the left of both stations. The signals for all three cases peak at exactly the same lag times due to
14
15
16 the constancy of group velocity, but the shape of the signal in Case 2 differs from that in Cases 1
17
18
19 and 3. This is due to the “initial phase” shift at all frequencies. On the other hand, no clear
20
21
22 difference in phase between Case 1 and Case 3 is observed. Background noise in the
23
24
25 cross-correlation is observed for all cases.
26
27
28
29
30
31
32
33

34 The phase velocity dispersion curves measured by FTAN are shown in **Figure 17b** for all three
35
36
37 cases. The medium is non-dispersive, so the group and phase speeds are the same. The velocity
38
39
40 dispersion curves for Case 1 and Case 2 confirm our method and the idea of how phase depends
41
42
43 on the source distribution. When $\lambda = 0$ and $\lambda = +\pi/4$ is applied to Case 1 and Case 2, respectively,
44
45
46 the measured phase velocities match the input phase velocity (3 km/s) at all periods with errors
47
48
49 less than 0.5%. At the same time, similar results are obtained when $\lambda = 0$ is used in Case 3,
50
51
52 although the source distribution is highly inhomogeneous. An example of the effect of using the
53
54
55 incorrect “initial phase” is also shown by using $\lambda = 0$ in Case 2. The measured phase velocity
56
57
58
59
60

1
2
3
4 dispersion curve clearly deviates from the input value and the error increases with period.
5
6
7
8
9

10
11
12 For comparison, the group velocity dispersion curves are also shown here in [Figure 17c](#) and
13
14 exhibit the intrinsic uncertainty difference between these two kinds of measurement. Group
15
16 velocity clearly exhibits higher uncertainty (up to ~ 2%) and the uncertainty tends to increase
17
18 with the period, although non-dispersive signals are particularly hard targets for group velocity
19
20 measurement. Note that the group velocity measurement is not λ dependent; hence even with
21
22 incorrect “initial phase”, $\lambda = 0$ for Case 2, the same measurement is returned.
23
24
25
26
27
28
29
30
31
32
33
34
35

36 Ambient noise source studies have concluded that the interaction between ocean waves and the
37
38 shallow sea floor is a major mechanism to create ambient noise. Other than a few special cases,
39
40 such as the 26 sec microseism in the Gulf of Guinea documented by Shapiro et al. (2006), there
41
42 is no evidence that ambient noise is generated exclusively in a highly localized area throughout a
43
44 long period of time. Several theoretical studies (e.g., Webb, 2007; Tanimoto, 2007) suggest that
45
46 ocean depth is a major factor in the strength of coupling between oceanic waves and the sea floor.
47
48
49
50
51
52 This results in a source distribution region distributed broadly in shallow off-shore regions of the
53
54
55
56
57
58
59
60

1
2
3
4 world's oceans, abstractly similar to what we suggest in Figure 16. In this case, the strength of
5
6
7 the source varies rather smoothly across the constructive interference region on both sides of the
8
9
10 station pair and the interference effect is nearly the same as if sources were homogeneously
11
12
13 distributed at all azimuths. We believe that this is the setting for most of our measurements, and
14
15
16 by setting $\lambda = 0$, the phase velocity is measured with considerable accuracy.
17
18
19
20
21
22
23
24

25 **6. Conclusion**

26
27
28
29 Continuous three-component ambient noise data obtained between Nov 1st 2005 and Oct 31st
30
31
32 2006 recorded by more than 250 stations in the Western United States were used to estimate both
33
34
35 Rayleigh and Love wave empirical Green's functions between every station-pair. On the
36
37
38 transverse-transverse cross-correlation function, the Love wave signal clearly emerges with an
39
40
41 average SNR higher than the Rayleigh wave particularly between 10 to 20 sec period. This
42
43
44 suggests that Love waves cannot be generated exclusively by the scattering of Rayleigh waves.
45
46
47 Above 20 sec period, the Love wave SNR drops off quickly, likely due to the increase in
48
49
50 incoherent local noise levels on the horizontal components. Further research is needed to
51
52
53 determine whether by combining with barometric or data, the local noise level can be
54
55
56 ameliorated and longer period Love wave empirical Green's functions can be obtained from
57
58
59
60

1
2
3
4 ambient noise.
5
6
7
8
9
10

11
12 Phase velocity dispersion between each station-pair was measured by frequency-time analysis
13
14 with the “initial phase”, λ , in equation (7) set to 0. The consistency and average uncertainty of
15
16 the measurements were determined by a novel three-station method. The results show that the
17
18 empirical Green’s functions can be estimated from the negative time derivative of the symmetric
19
20 component cross-correlation function without major bias and with the average uncertainty of the
21
22 travel time is around 1 second for periods shorter than 24 sec. The Rayleigh and Love wave
23
24 phase velocity maps at four periods, 8, 12, 16 and 20 sec, were constructed and show reasonable
25
26 qualitative agreement with known geological features and with previous studies. The large
27
28 velocity variations present in the maps together with systematic errors observed in the
29
30 three-station analysis suggest that both off-great-circle and finite frequency effects should be
31
32 considered when a future tomography is performed for azimuthal anisotropy. Future inversion of
33
34 these data to produce a 3-D crustal model of the western United States with radial anisotropy is a
35
36 natural extension of this study.
37
38
39
40
41
42
43
44
45
46
47
48
49
50
51
52
53
54
55
56
57
58
59
60

Acknowledgements

The data used in this research were obtained from the IRIS Data Management Center and originate predominantly from the Transportable Array component of USArray. The authors are grateful to Toshiro Tanimoto and two anonymous reviewers for comments that helped to improve this paper. This research was supported by a grant from the US National Science Foundation, grant EAR-0450082, and a contract from the US Department of Energy, contract DE-FC52-2005NA2607. MPM acknowledges a National Defense Science and Engineering Graduate Fellowship from the American Society for Engineering Education.

Reference List

- Barmin, M.P., Ritzwoller, M.H. & Levshin, A.L., 2001. A fast and reliable method for surface wave tomography, *Pure Appl. Geophys.*, 158, 1351-1375.
- Bensen, G.D., Ritzwoller, M.H., Barmin, M.P., Levshin, A.L., Lin, F., Moschetti, M.P., Shapiro, N.M., & Yang, Y., 2007a. Processing seismic ambient noise data to obtain reliable broad-band surface wave dispersion measurements, *Geophys. J. Int.*, 10.1111/j.1365-246X.2007.03374.x.

1
2
3
4 Bensen, G.D., Ritzwoller, M.H., & Shapiro, N.M., 2007b. Broad-band ambient noise surface
5
6
7 wave tomography across the United States, *J. Geophys. Res.*, submitted.
8
9

10
11 Campillo, M. & Paul, A., 2003. Long-range correlations in the diffuse seismic coda, *Science*, 299,
12
13
14 547-549.
15
16

17
18
19 Kang, T.S. & Shin, J.S., 2006. Surface-wave tomography from ambient seismic noise of
20
21
22 accelerograph networks in southern Korea, *Geophys.Res.Lett.*, 33, L17303.
23
24

25
26 Lin, F.C, Ritzwoller, M.H., Townend, J., Savage, M., & Bannister, S., 2007, Ambient noise
27
28
29 Rayleigh wave tomography of New Zealand, *Geophys. J. Int.*, 18 pages,
30
31
32 doi:10.1111/j.1365-246X.2007.03414.x, 2007.
33
34

35
36 Levshin, A.L., Barmin, M.P., Ritzwoller, M.H. & Trampert, J. 2005. Minor-arc and major-arc
37
38
39 global surface wave diffraction tomography, *Phys. Earth Planet. Int.*, **149**, 205–223.
40

41
42 Lobkis, O.I. & Weaver, R.L., 2001. On the emergence of the Green's function in the correlations
43
44
45 of a diffuse field, *J.Acoust.Soc.Am.*, 110, 3011-3017.
46
47

48
49 Moschetti, M.P., Ritzwoller, M.H., & Shapiro, N.M., Surface wave tomography of the western
50
51
52 United States from ambient seismic noise: Rayleigh wave group velocity maps, *Geochem.,*
53
54
55 *Geophys., Geosys.*, 8, Q08010, doi:10.1029/2007GC001655.
56
57
58
59
60

- 1
2
3
4 Paul, A., Campillo, M., Margerin, L., Larose, E., & Derode, A., 2005. Empirical synthesis of
5
6
7 time-asymmetrical Green functions from the correlation of coda waves, *J. Geophys. Res.*,
8
9
10 110, B08302.
11
12
13
14 Rhie, J. & Romanowicz, B., 2006. A study of the relation between ocean storms and the Earth's
15
16
17 hum, *Geochem., Geophys., Geosys.*, 7, Q10004.
18
19
20
21 Rhie, J. & Romanowicz, B., 2004. Excitation of Earth's continuous free oscillations by
22
23
24 atmosphere-ocean-seafloor coupling, *Nature*, 431, 552-556.
25
26
27
28
29 Ritzwoller, M.H., Shapiro, N.M., Barmin, M.P., & Levshin, A.L., 2002. Global surface wave
30
31
32 diffraction tomography, *J. Geophys. Res.*, 107, 2335.
33
34
35
36 Roux, P., Sabra, K.G., Kuperman, W.A., & Roux, A., 2005. Ambient noise cross correlation in free
37
38
39 space: Theoretical approach, *J. Acoust. Soc. Am.*, 117, 79-84.
40
41
42
43 Sabra, K.G., Gerstoft, P., Roux, P., Kuperman, W.A., & Fehler, M.C., 2005a. Surface wave
44
45
46 tomography from microseisms in Southern California, *Geophys. Res. Lett.*, 32, L14311.
47
48
49
50 Sabra, K.G., Roux, P. & Kuperman, W.A., 2005b. Emergence rate of the time-domain Green's
51
52
53 function from the ambient noise cross-correlation function, *J. Acoust. Soc. Am.*, 118,
54
55
56 3524-3531.
57
58
59
60

- 1
2
3
4 Shapiro, N.M., Campillo, M., Stehly, L., & Ritzwoller, M.H., 2005. High-resolution
5
6
7 surface-wave tomography from ambient seismic noise, *Science*, 307, 1615-1618.
8
9
10
11 Shapiro, N.M., Ritzwoller, M.H. & Bensen, G.D., 2006. Source location of the 26 sec
12
13
14 microseism from cross-correlations of ambient seismic noise, *Geophys.Res.Lett.*, 33,
15
16
17 L18310.
18
19
20
21 Shapiro, N.M., Ritzwoller, M.H., Molnar, P., & Levin, V., 2004. Thinning and flow of Tibetan
22
23
24 crust constrained by seismic anisotropy, *Science*, 305, 233-236.
25
26
27
28
29 Snieder, R., 2004. Extracting the Green's function from the correlation of coda waves: A
30
31
32 derivation based on stationary phase, *Physical Review E*, 69, 046610.
33
34
35
36 Stehly, L., Campillo, M. & Shapiro, N.M., 2006. A study of the seismic noise from its long-range
37
38
39 correlation properties, *J. Geophys. Res.*, 111, B10306.
40
41
42
43 Tanimoto, T., 2007. Excitation of normal modes by non-linear interaction of ocean waves,
44
45
46
47 *Geophys. J. Int.*, 168, 571-582.
48
49
50
51 Webb, S.C., 2007. The Earth's 'hum' is driven by ocean waves over the continental shelves,
52
53
54
55
56
57
58
59
60

1
2
3
4 Yang, Y. & Forsyth, D.W., 2006. Rayleigh wave phase velocities, small-scale convection, and
5
6 azimuthal anisotropy beneath southern California, *J. Geophys. Res.*, 111, B07306.
7
8

9
10
11 Yang, Y. & Ritzwoller, M.H., 2007. The characteristics of seismic noise as a source for ambient
12
13 noise tomography, *Geochem., Geophys., Geosys.*, submitted.
14
15
16

17
18 Yang, Y., Ritzwoller, M.H., Levshin, A.L. & Shapiro, N.M., 2007. Ambient noise Rayleigh wave
19
20 tomography across Europe, *Geophys. J. Int.*, 168, 259-274.
21
22
23

24
25 Yao, H.J., van der Hilst, R.D. & de Hoop, M.V., 2006. Surface-wave array tomography in SE
26
27 Tibet from ambient seismic noise and two-station analysis - I. Phase velocity maps,
28
29
30
31
32
33
34
35
36
37
38
39
40
41
42
43
44
45
46
47
48
49
50
51
52
53
54
55
56
57
58
59
60

Geophys. J. Int., 166, 732-744.

Figure Captions

Figure 1. Location of the 253 broadband stations used in this study, most from the Transportable Array component of USArray. The color indicates the duration of the deployment during this study.

Figure 2. Illustration of how transverse and radial components are defined between two stations.

Figure 3. The 10-25 sec band-pass filtered cross-correlations observed between two

1
2
3
4 EarthScope/USArray TA stations, 116A (Eloy, Arizona) and R06C (Coleville, California). The
5
6
7 prediction windows used for SNR analysis, defined for arrivals with velocities between 2 and 5
8
9
10 km/s, are marked in gray. Z, R, and T denote vertical, radial, and transverse, respectively.
11
12
13

14 **Figure 4.** The 10-50 sec band-pass filtered cross-correlation record section centered at station
15
16
17 MOD (Modoc Plateau, California) with (a) vertical-vertical cross-correlations and (b)
18
19
20 transverse-transverse cross-correlations. The dashed lines in (a) and (b) indicate the 3.0 km/s and
21
22
23 3.3 km/s move-out, respectively. Only the station pairs with SNR higher than 20 at 18 sec period
24
25
26 are plotted here.
27
28
29
30

31 **Figure 5.** The average SNR for Rayleigh and Love waves. Only station pairs separated by a
32
33
34 distance greater than three wavelengths contributed to the average.
35
36
37

38 **Figure 6.** (a) Preliminary phase velocity dispersion curves between stations CVS (Carmenet
39
40
41 Vineyards, Sonoma, California) and VES (Vestal, Porterville, California), with various different
42
43
44 values of the phase ambiguity factor N in equation (7). The inter-station distance is 409 km. The
45
46
47 green lines show the result with the value of N off by ± 1 . The red line shows the dispersion
48
49
50 measurement obtained by FTAN and the black line is the reference dispersion curve. The
51
52
53 Rayleigh wave is shown with solid lines and the Love wave is shown with dash lines. (b) The
54
55
56 Love wave dispersion curve after the 1st and 2nd measurement. Both the preliminary and the
57
58
59
60

revised reference curves are shown. The preliminary dispersion measurement is plotted as a dashed green line and the revised dispersion measurement is plotted as a solid red line.

Figure 7. (a) Location of stations O01C, R04C, ORV, and TIN. (b) The 5–40 sec band-pass filtered symmetric cross-correlations for the vertical–vertical component (Z-Z) and the transverse–transverse component (T-T). (c) The measured Rayleigh and Love wave dispersion curves based on the symmetric cross-correlations shown in (b). The preliminary reference dispersion curves for both Rayleigh and Love wave are shown as green solid and dashed lines, respectively.

Figure 8. (a) Definition of the inter-station distances d_1 , d_2 , and d_3 used in the three-station analysis of the phase velocity measurements. (b) The relationship observed between distance difference, Δd , and phase travel time difference, Δt , where the red dots mark individual observations from 40,782 station-triples. (c) The relationship between distance difference, Δd , and the corrected phase travel time difference, $\Delta t'$, when $\lambda=0$. (d) Same as (c), but $\lambda=-\pi/4$ is used.

Figure 9. (a) & (b) The histograms of corrected phase travel time difference, $\Delta t'$, with $\lambda=0$ for Rayleigh and Love waves. The best fit Gaussian curves are also shown. (c) & (d) Same as (a) & (b), but $\lambda=-\pi/4$ is used for comparison.

1
2
3
4 **Figure 10.** The number of phase velocity measurements satisfying the far-field approximation
5
6
7 and the high SNR criterion are presented as a function of period and compared.
8
9

10
11 **Figure 11.** (a) & (c) The ray path coverage by the 12 sec Rayleigh and Love wave phase velocity
12
13 data sets, respectively. (b) & (d) The 12 sec resolution maps for Rayleigh and Love waves,
14
15 respectively, where resolution is defined as twice the standard deviation of a 2-D Gaussian
16
17 function fit to the resolution matrix at each point. The 100 km resolution contour is shown with a
18
19 thick black line.
20
21
22
23
24
25
26
27

28 **Figure 12.** The estimated Rayleigh wave phase velocity maps at periods of 8 sec, 12 sec, 16 sec,
29
30 and 20 sec. The 100 km resolution contour is shown for reference.
31
32
33
34

35 **Figure 13.** The estimated Love wave phase velocity maps at periods of 8 sec, 12 sec, 16 sec, and
36
37 20 sec. The 100 km resolution contour is shown for reference.
38
39
40
41

42 **Figure 14.** Travel time misfit histograms for the tomography maps shown in Figures 12 and 13.
43
44 The standard deviation (STDV) of misfit is also presented.
45
46
47
48

49 **Figure 15.** Vertical phase velocity sensitivity kernels of Rayleigh and Love waves at periods of 8,
50
51 12, 16, and 20 sec, calculated with the 1D PREM model in which the ocean is replaced by a
52
53 sedimentary layer.
54
55
56
57
58
59
60

1
2
3
4 **Figure 16.** An example of iso-phase hyperbolas each separated from its nearest neighbor by $\pm\pi$.

5
6
7 A phase velocity of 3 km/s for 50 sec period is used to construct the hyperbolas. The same setup
8
9 parameters were used for the synthetic experiments. The gray area defines the region over which
10
11 sources were randomly distributed for the synthetic experiment referred to as Case 3.
12
13
14
15

16
17 **Figure 17.** (a) The synthetic cross-correlations recovered for Cases 1, 2 and 3. (b) The phase
18
19 velocity dispersion curves result from the estimated Green's functions derived from the synthetic
20
21 cross-correlations in (a). Two "initial phase" values, 0 and $\pi/4$, are used to obtain the phase
22
23 velocity dispersion curve for Case 2. Nearly correct phase velocity, 3 km/s, is returned when the
24
25 correct "initial phase" is applied. (c) The measured group velocity dispersion curves for Cases 1,
26
27
28
29
30
31
32
33 2, and 3.
34
35
36
37
38
39
40
41
42
43
44
45
46
47
48
49
50
51
52
53
54
55
56
57
58
59
60

Table 1. The summary of the three-station analysis.

	Rayleigh Wave						Love Wave			
	$\lambda=0$			$\lambda=-\pi/4$			$\lambda=0$		$\lambda=-\pi/4$	
	12 s	18 s	24 s	12 s	18 s	24 s	12 s	18 s	12 s	18 s
$\overline{\Delta t'}$ (s)	0.056	0.262	0.337	1.535	2.486	3.291	0.237	0.409	1.718	2.631
σ (s)	0.912	1.127	1.372	0.922	1.139	1.381	0.945	1.144	0.952	1.159

For Peer Review

1
2
3
4
5
6
7
8
9
10
11
12
13
14
15
16
17
18
19
20
21
22
23
24
25
26
27
28
29
30
31
32
33
34
35
36
37
38
39
40
41
42
43
44
45
46
47
48
49
50
51
52
53
54
55
56
57
58
59
60

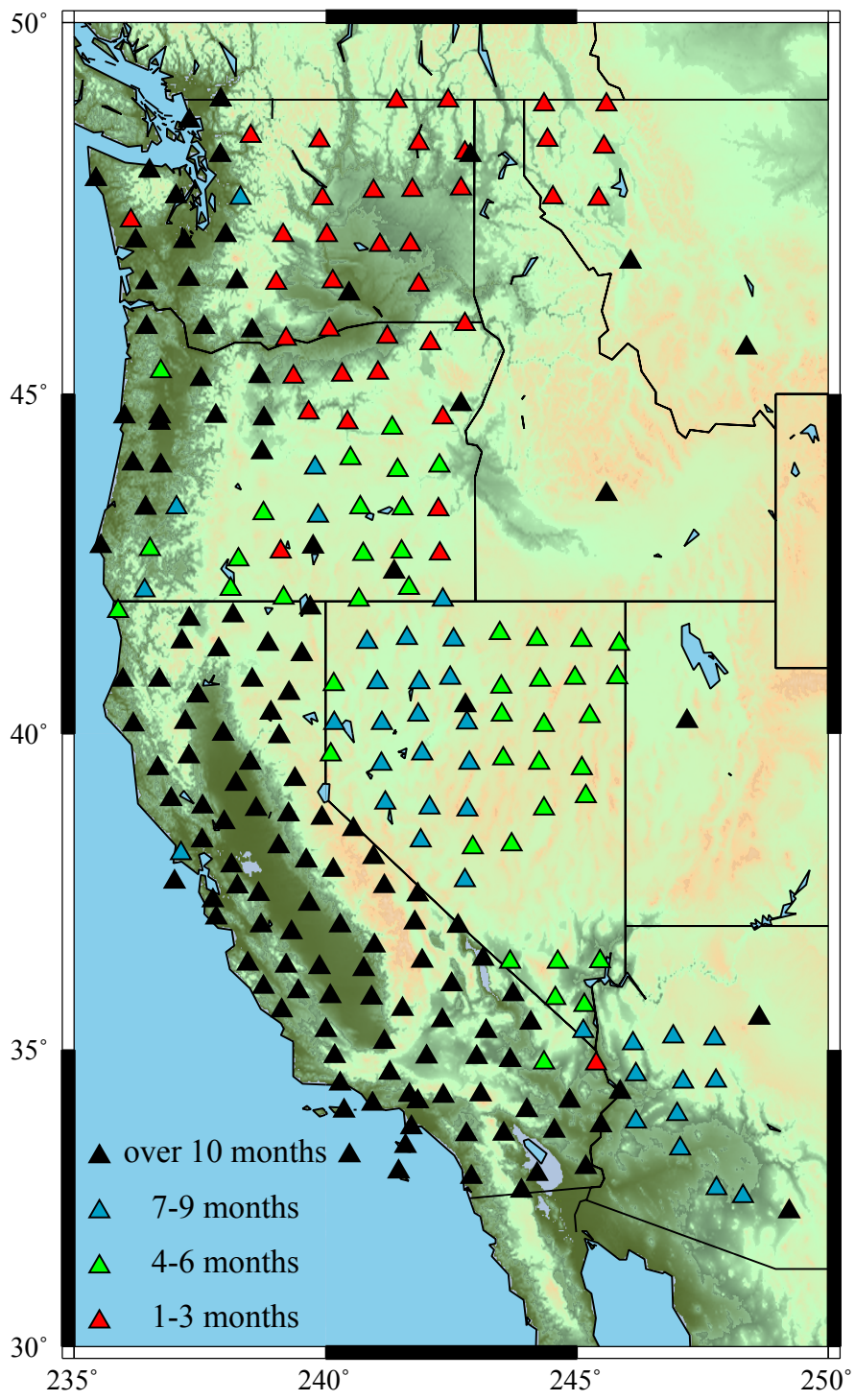


Figure 1.

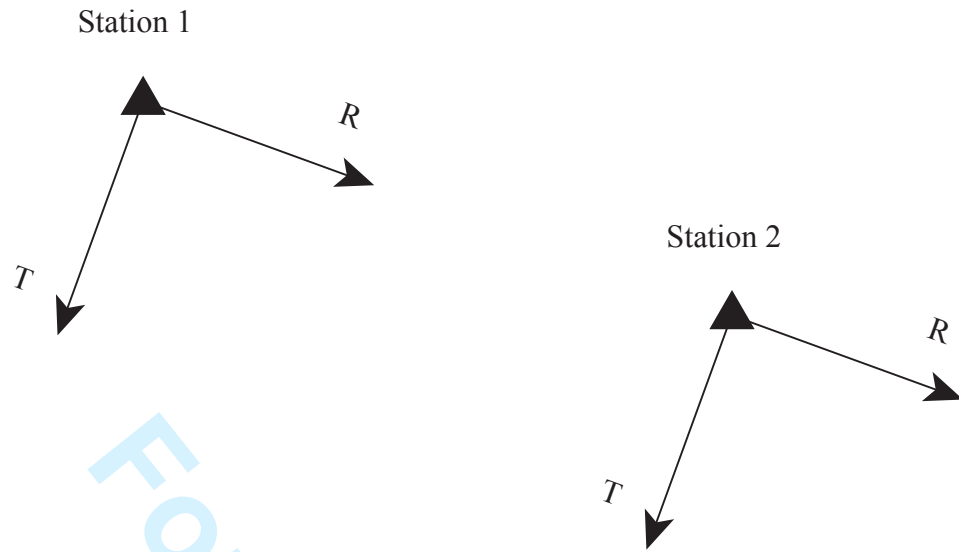


Figure 2.

For Peer Review

1
2
3
4
5
6
7
8
9
10
11
12
13
14
15
16
17
18
19
20
21
22
23
24
25
26
27
28
29
30
31
32
33
34
35
36
37
38
39
40
41
42
43
44
45
46
47
48
49
50
51
52
53
54
55
56
57
58
59
60

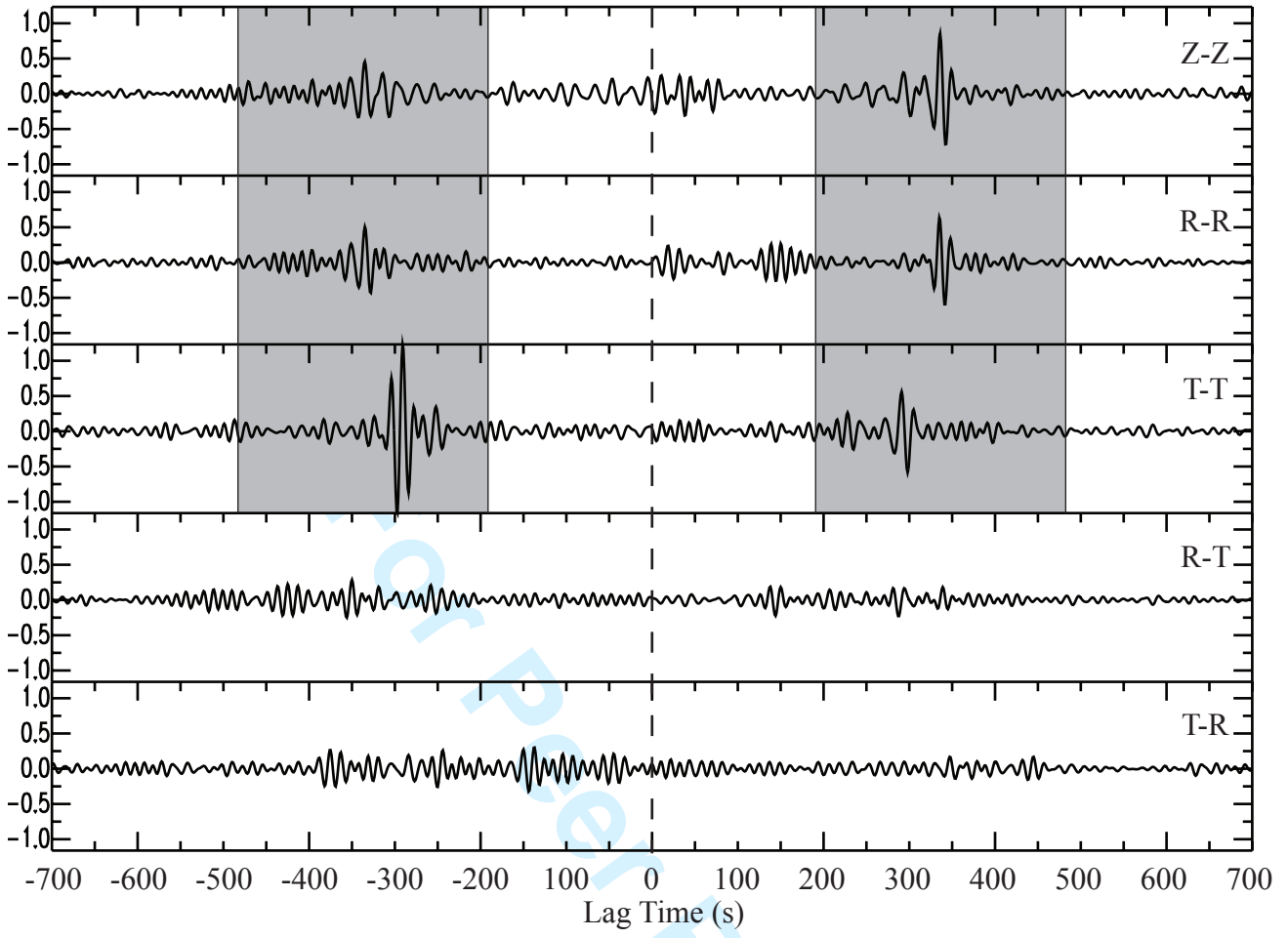


Figure 3

1
2
3
4
5
6
7
8
9
10
11
12
13
14
15
16
17
18
19
20
21
22
23
24
25
26
27
28
29
30
31
32
33
34
35
36
37
38
39
40
41
42
43
44
45
46
47
48
49
50
51
52
53
54
55
56
57
58
59
60

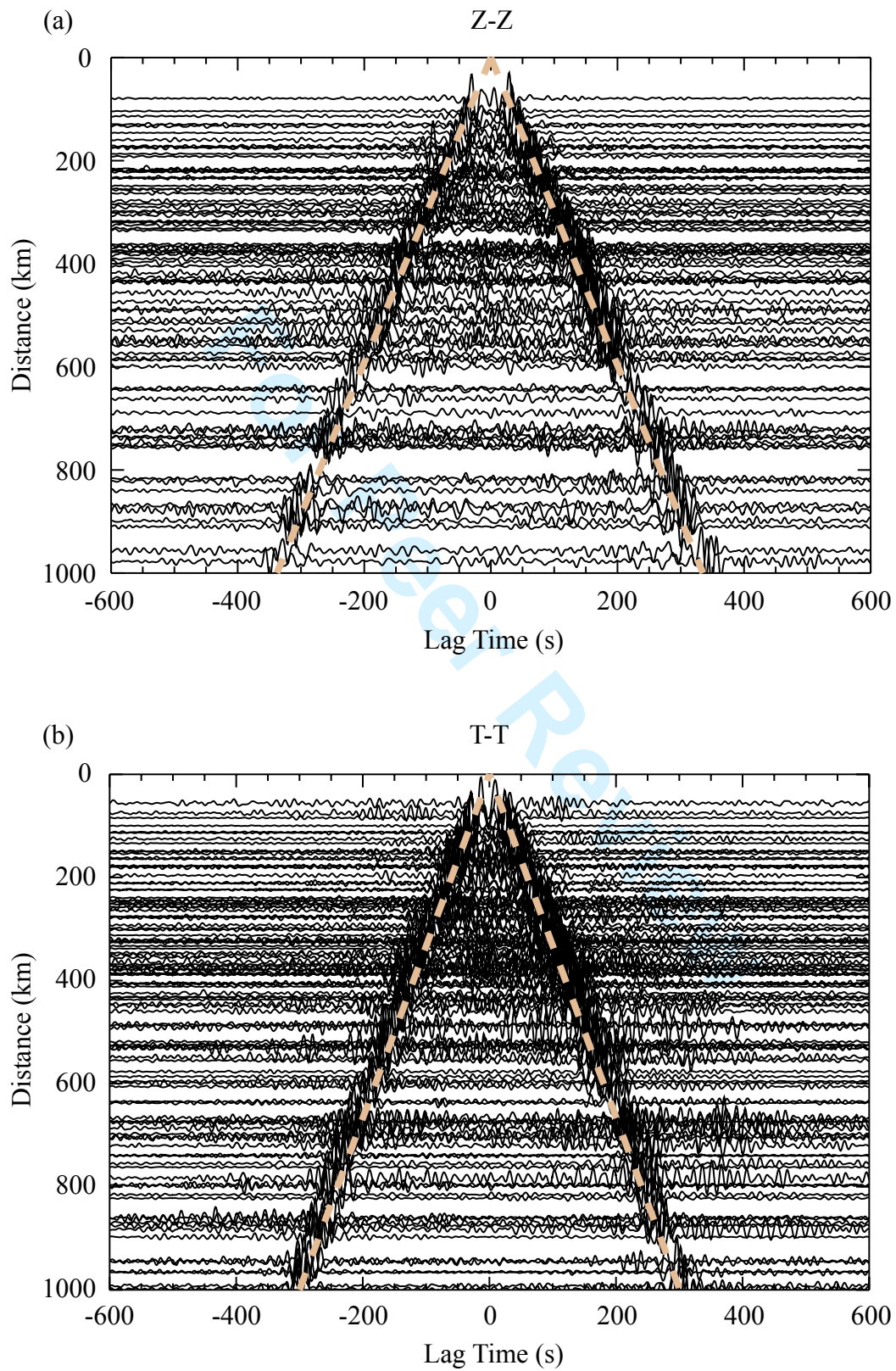


Figure 4.

1
2
3
4
5
6
7
8
9
10
11
12
13
14
15
16
17
18
19
20
21
22
23
24
25
26
27
28
29
30
31
32
33
34
35
36
37
38
39
40
41
42
43
44
45
46
47
48
49
50
51
52
53
54
55
56
57
58
59
60

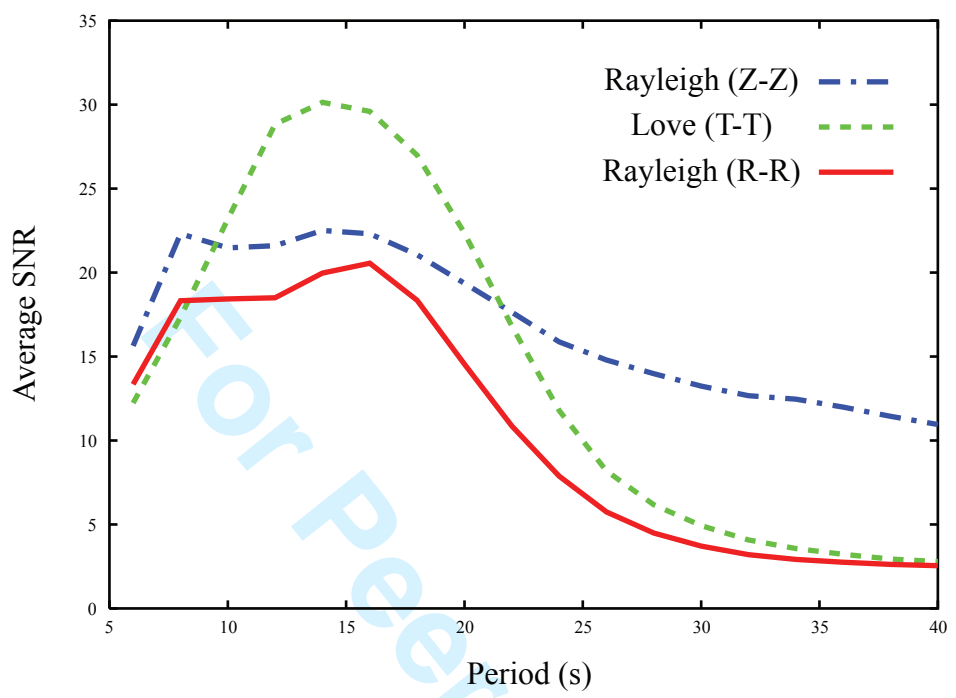


Figure 5

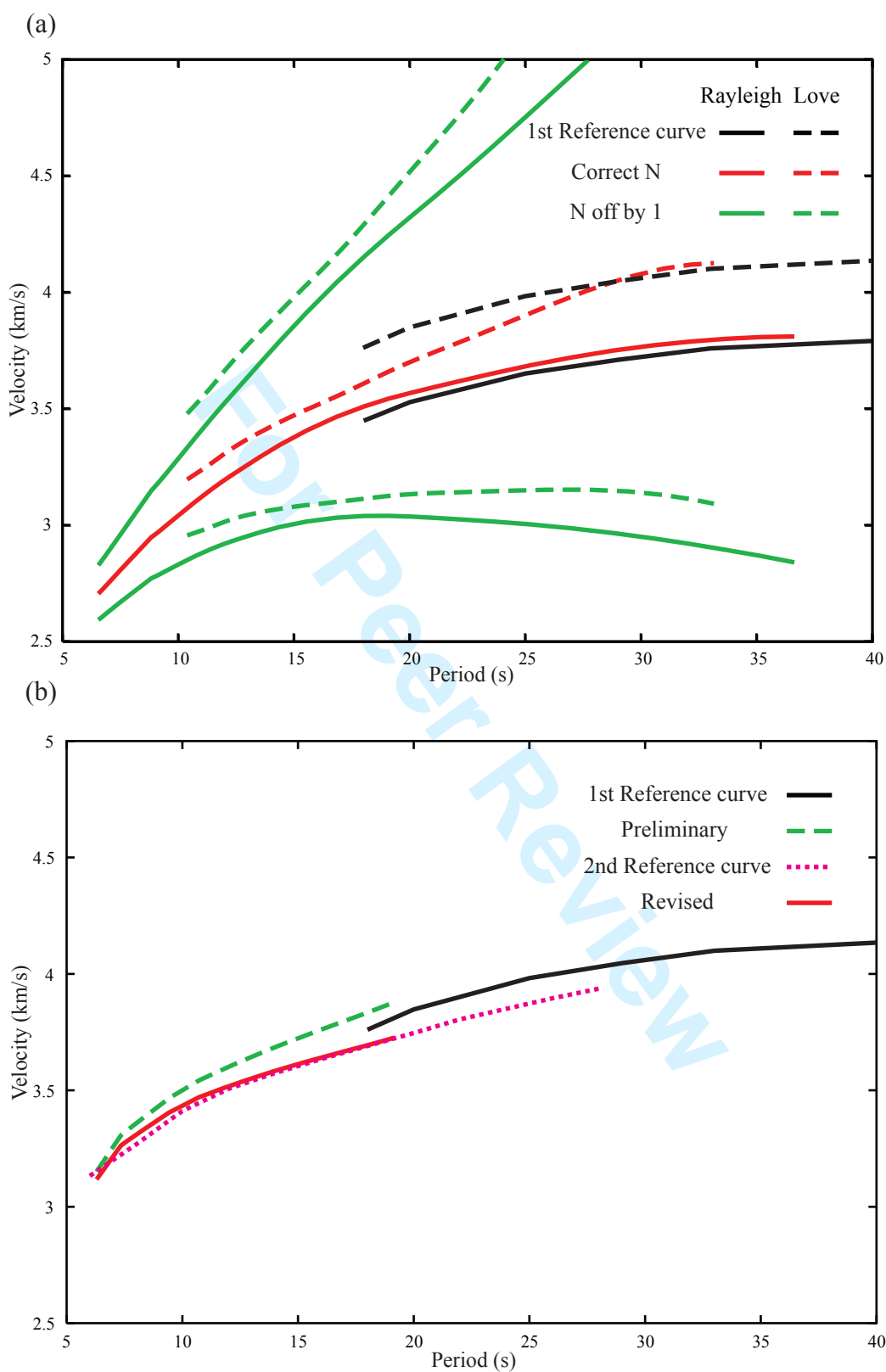


Figure 6.

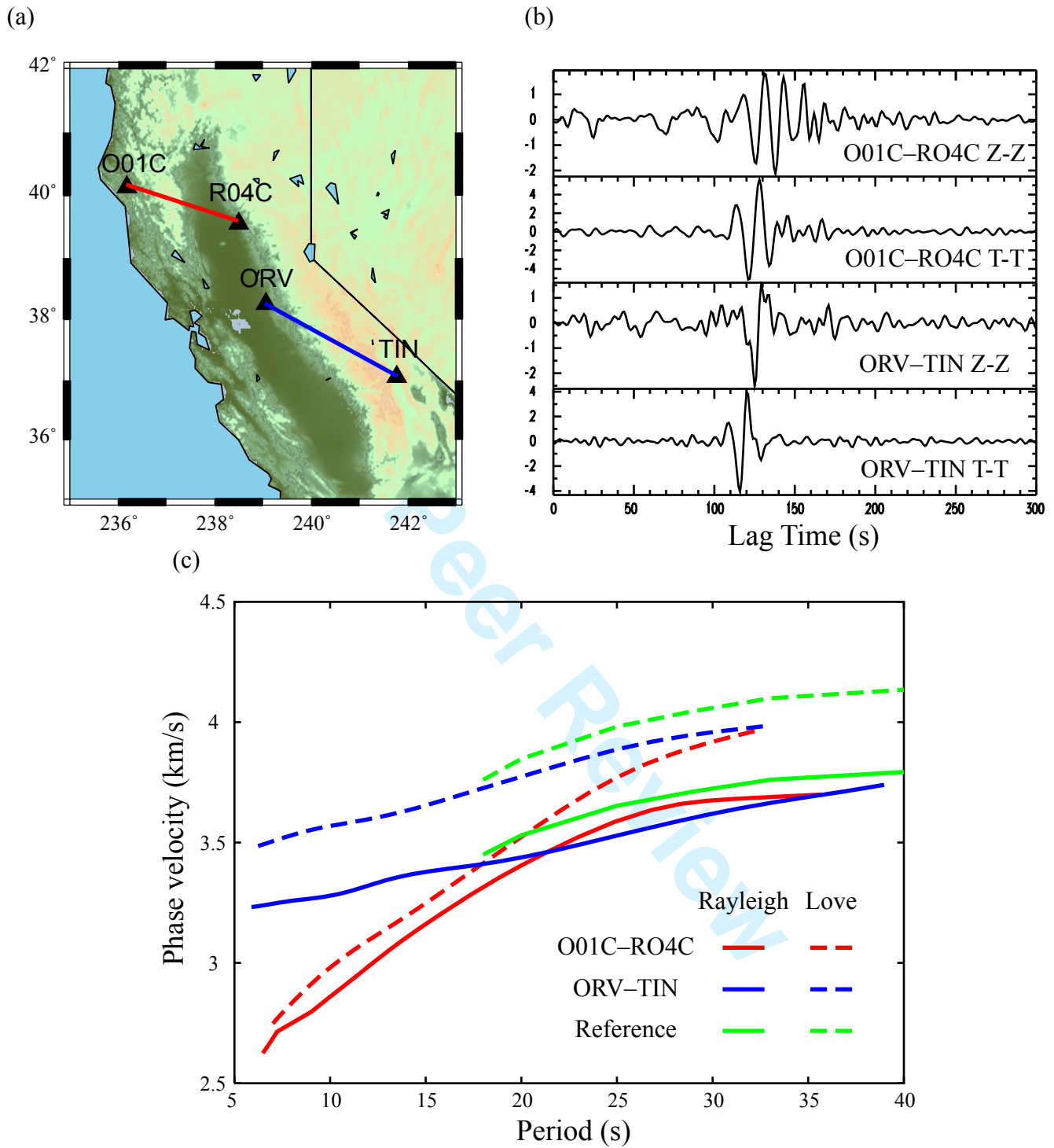


Figure 7.

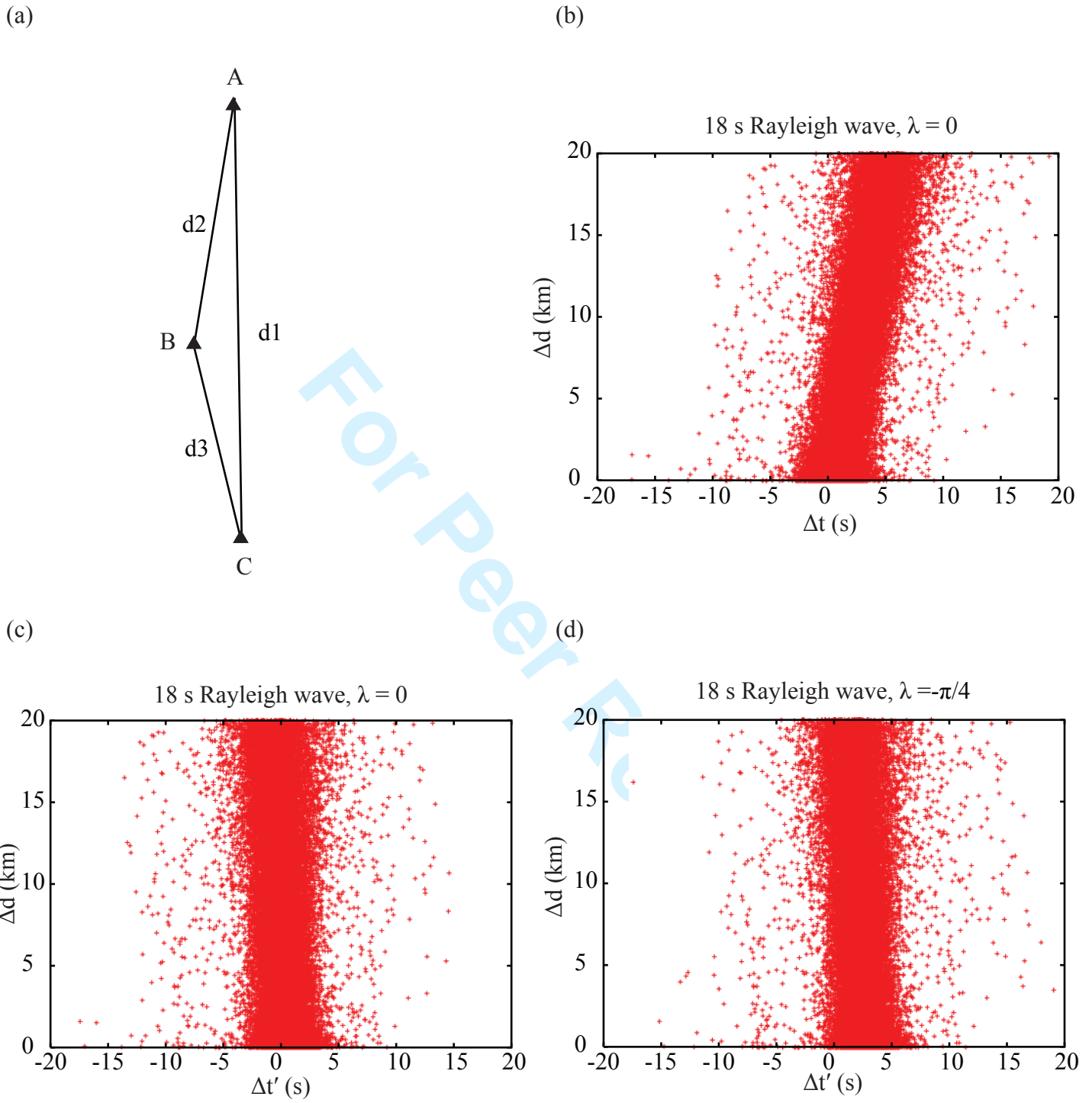


Figure 8

1
2
3
4
5
6
7
8
9
10
11
12
13
14
15
16
17
18
19
20
21
22
23
24
25
26
27
28
29
30
31
32
33
34
35
36
37
38
39
40
41
42
43
44
45
46
47
48
49
50
51
52
53
54
55
56
57
58
59
60

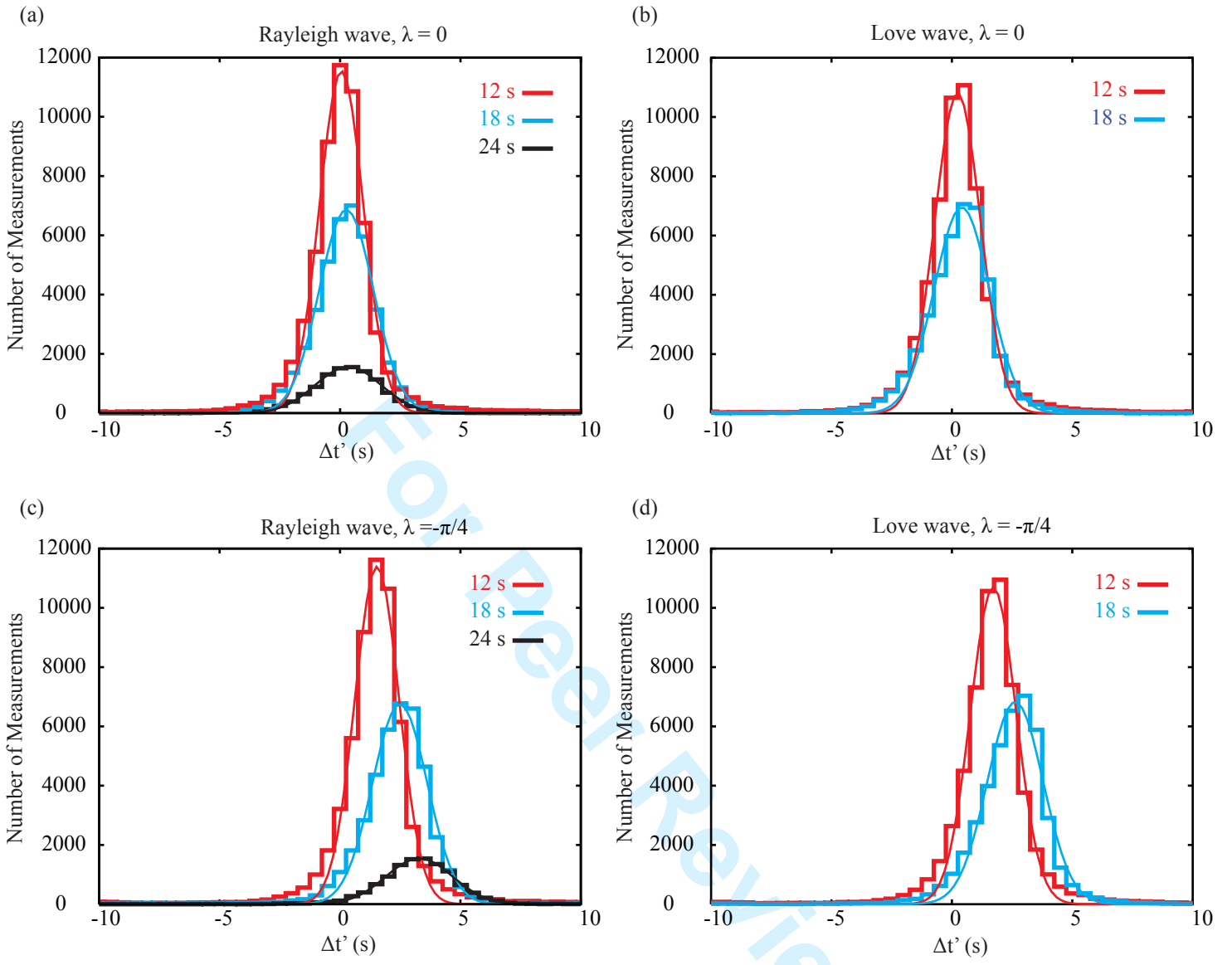


Figure 9.

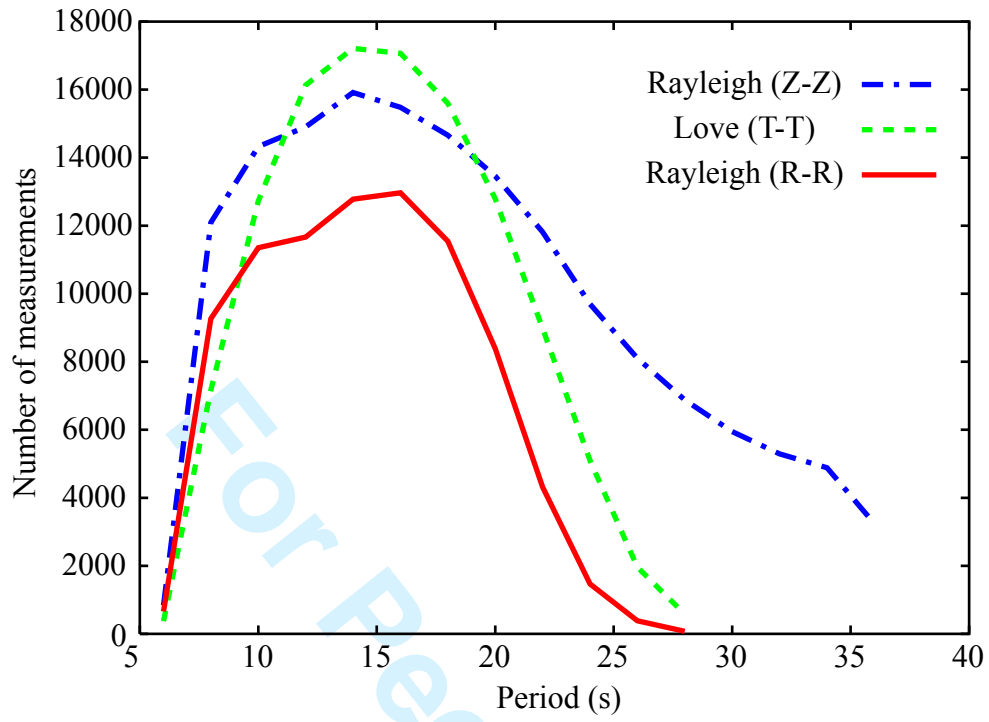


Figure 10.

1
2
3
4
5
6
7
8
9
10
11
12
13
14
15
16
17
18
19
20
21
22
23
24
25
26
27
28
29
30
31
32
33
34
35
36
37
38
39
40
41
42
43
44
45
46
47
48
49
50
51
52
53
54
55
56
57
58
59
60

1
2
3
4
5
6
7
8
9
10
11
12
13
14
15
16
17
18
19
20
21
22
23
24
25
26
27
28
29
30
31
32
33
34
35
36
37
38
39
40
41
42
43
44
45
46
47
48
49
50
51
52
53
54
55
56
57
58
59
60

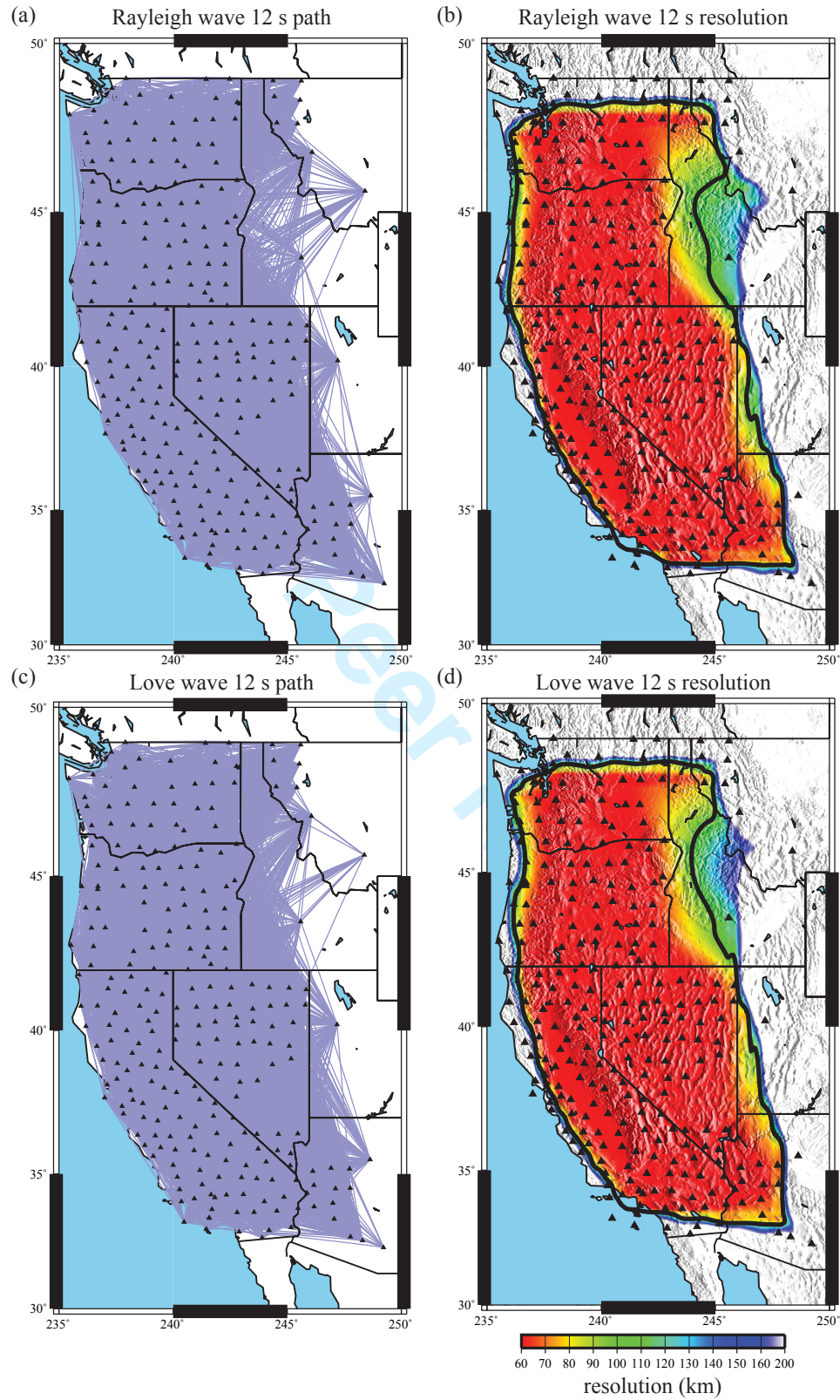


Figure 11.

1
2
3
4
5
6
7
8
9
10
11
12
13
14
15
16
17
18
19
20
21
22
23
24
25
26
27
28
29
30
31
32
33
34
35
36
37
38
39
40
41
42
43
44
45
46
47
48
49
50
51
52
53
54
55
56
57
58
59
60

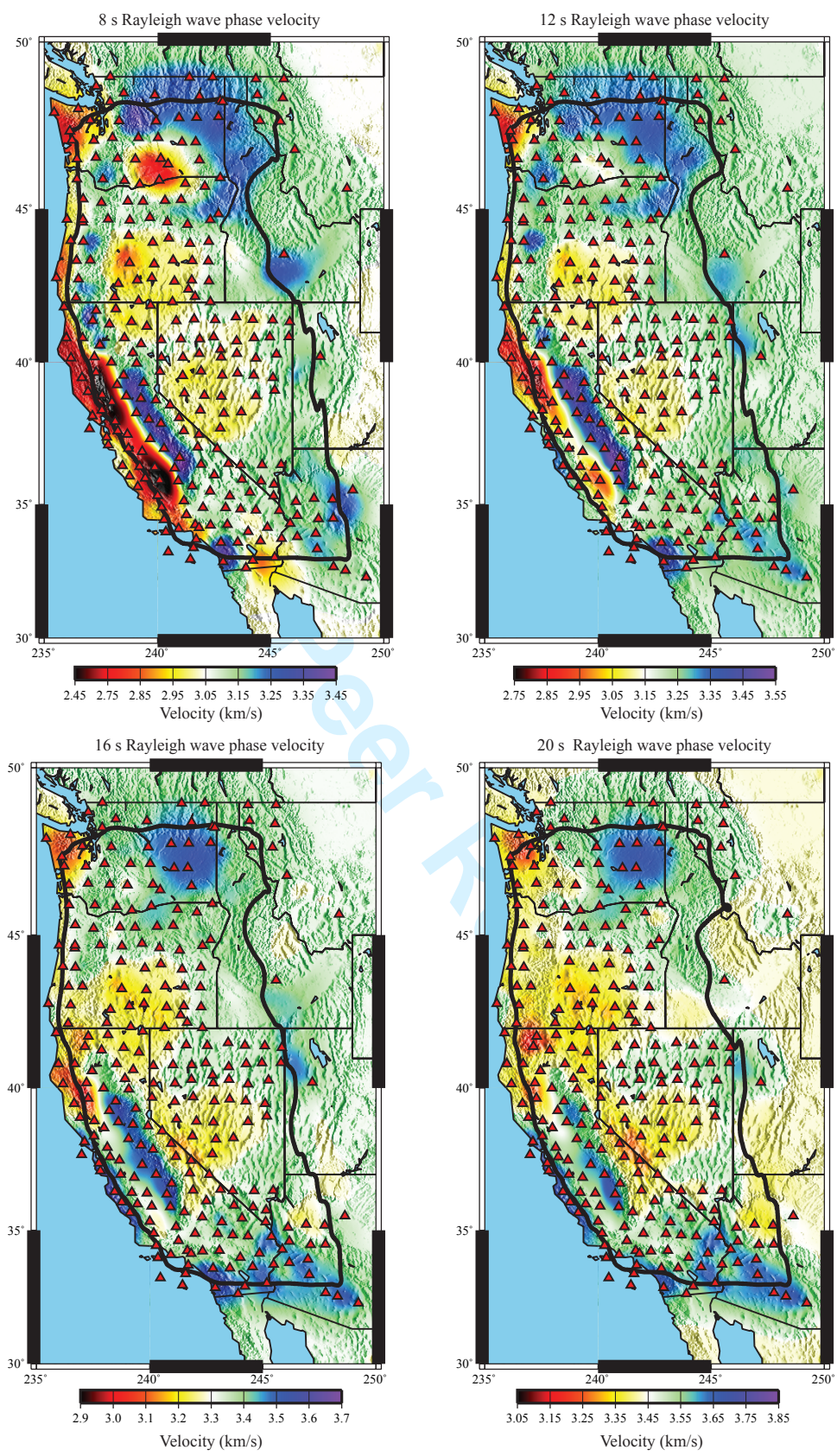


Figure 12

1
2
3
4
5
6
7
8
9
10
11
12
13
14
15
16
17
18
19
20
21
22
23
24
25
26
27
28
29
30
31
32
33
34
35
36
37
38
39
40
41
42
43
44
45
46
47
48
49
50
51
52
53
54
55
56
57
58
59
60

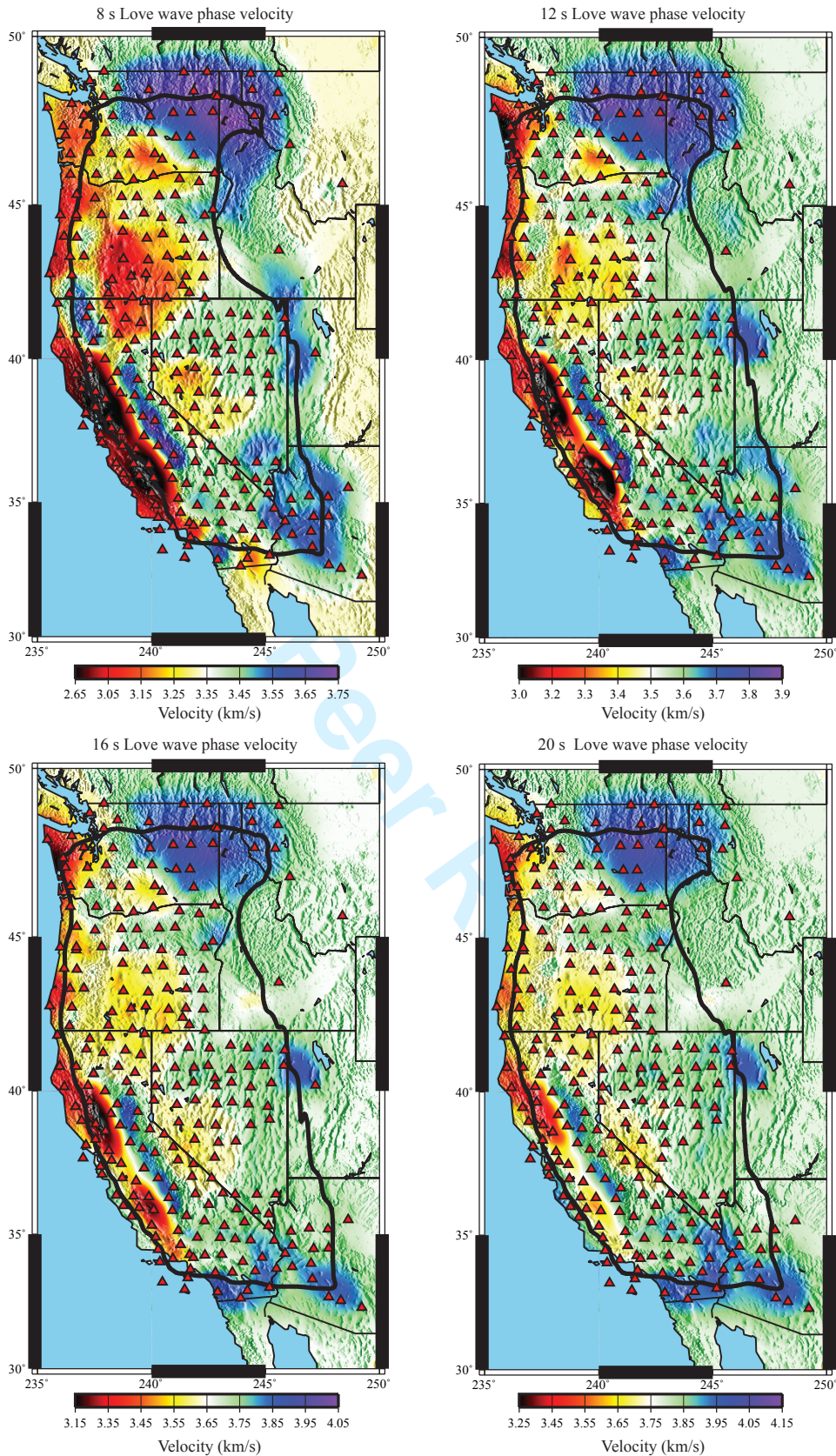


Figure 13

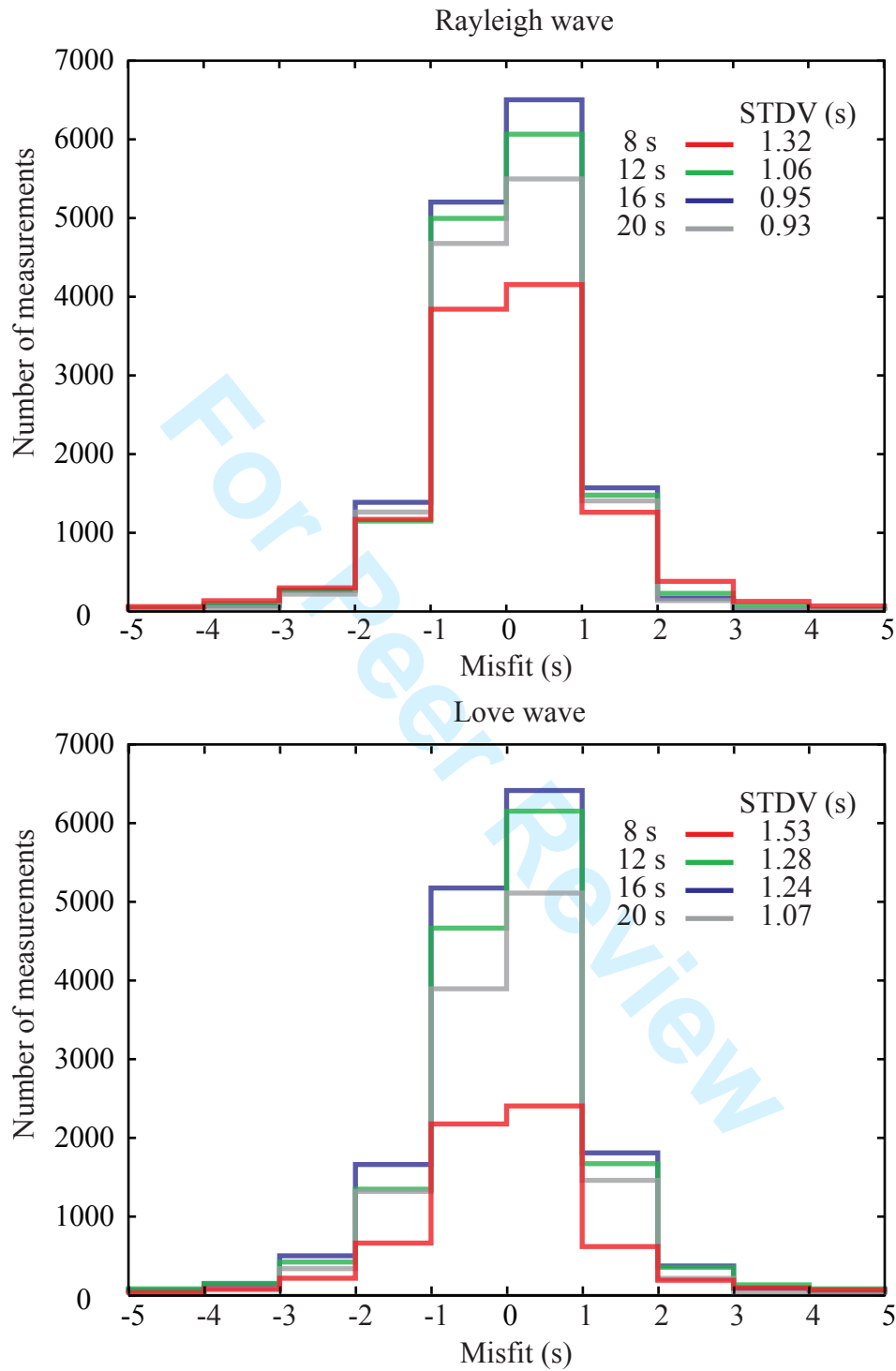


Figure 14

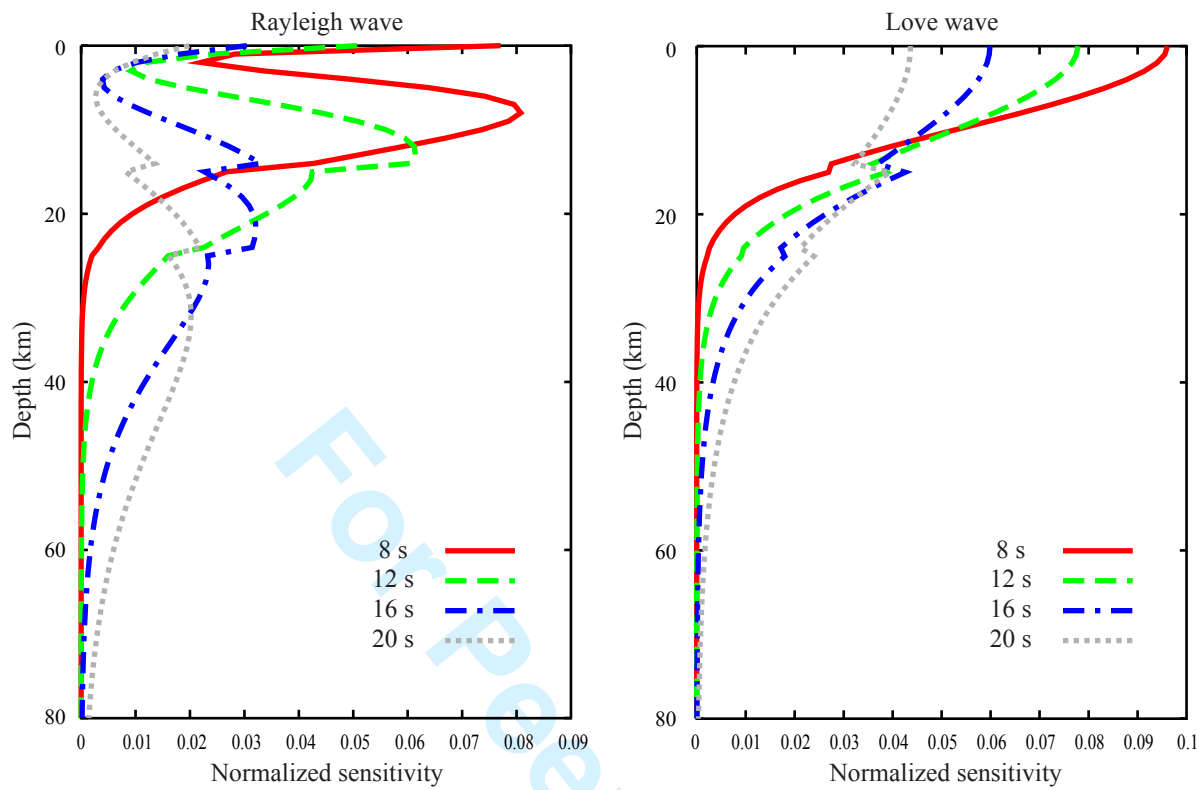


Figure 15

1
2
3
4
5
6
7
8
9
10
11
12
13
14
15
16
17
18
19
20
21
22
23
24
25
26
27
28
29
30
31
32
33
34
35
36
37
38
39
40
41
42
43
44
45
46
47
48
49
50
51
52
53
54
55
56
57
58
59
60

1
2
3
4
5
6
7
8
9
10
11
12
13
14
15
16
17
18
19
20
21
22
23
24
25
26
27
28
29
30
31
32
33
34
35
36
37
38
39
40
41
42
43
44
45
46
47
48
49
50
51
52
53
54
55
56
57
58
59
60

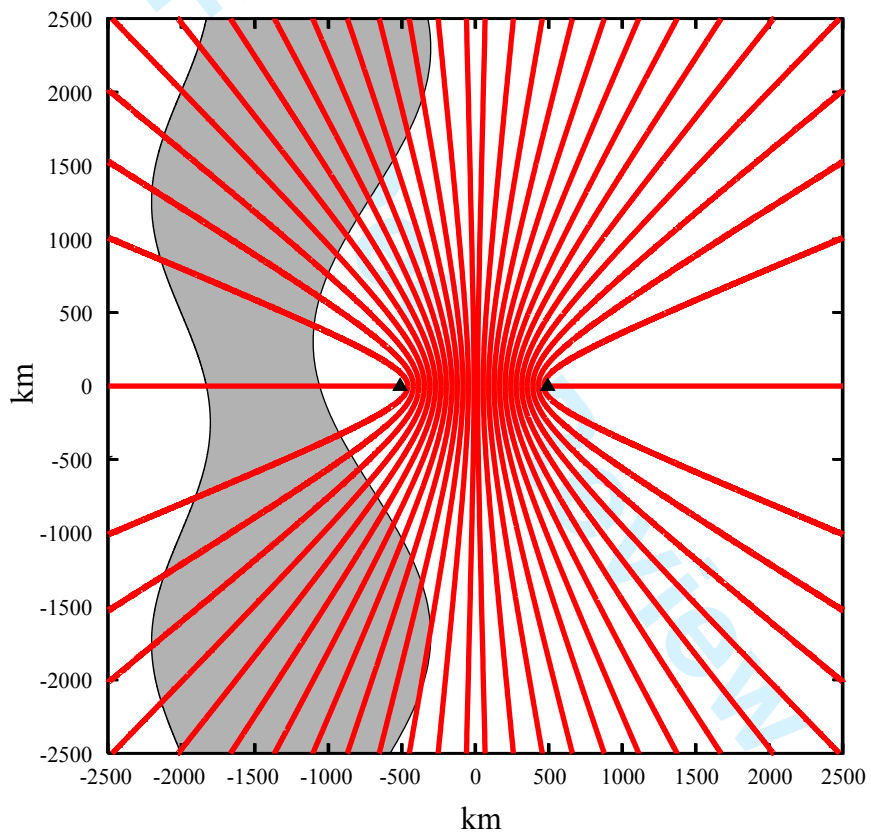


Figure 16.

1
2
3
4
5
6
7
8
9
10
11
12
13
14
15
16
17
18
19
20
21
22
23
24
25
26
27
28
29
30
31
32
33
34
35
36
37
38
39
40
41
42
43
44
45
46
47
48
49
50
51
52
53
54
55
56
57
58
59
60

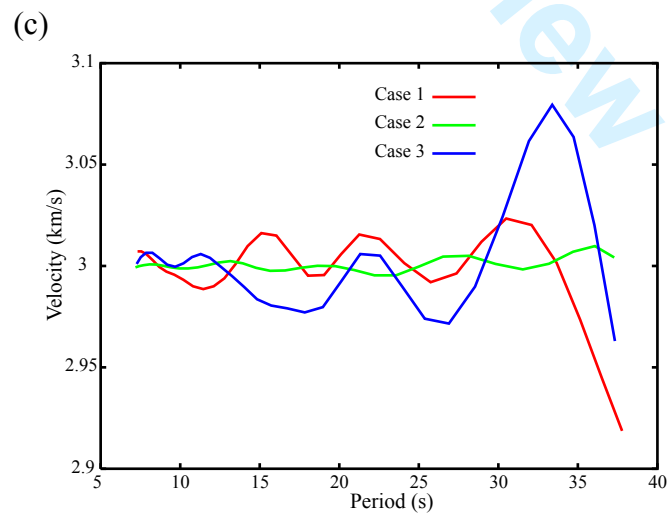
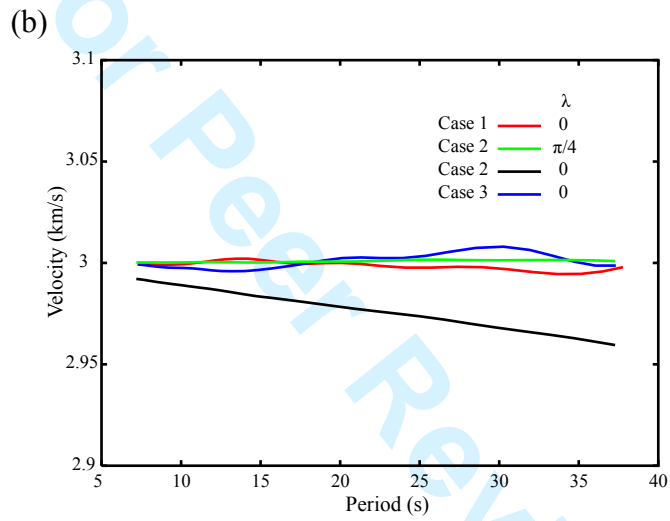
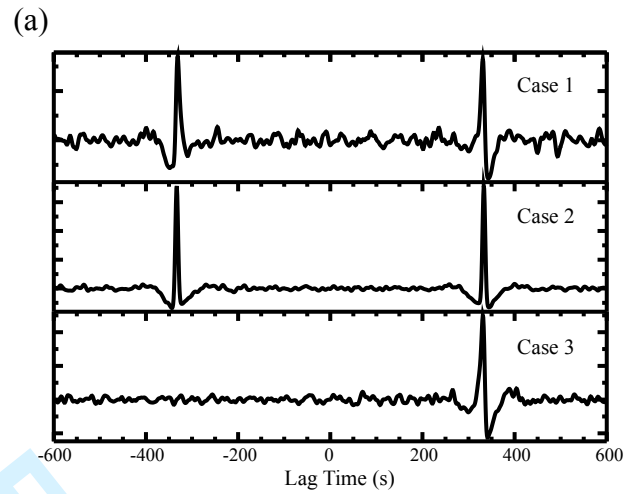


Figure 17.